Deformation of a biconcave-discoid capsule in extensional flow and electric field

Sudip Das[1], **Shivraj D. Deshmukh**[1] **and Rochish M. Thaokar**[1],†

[1]Department of Chemical Engineering, Indian Institute of Technology Bombay, Mumbai, 400076, India

Natural (red blood cells) and artificial biconcave-discoid-shaped capsules have immense biological (a cellular component of blood) and technological (as drug carrier) relevance, respectively. Their low reduced volume allows significant shape changes under external fields such as extensional flows (encountered at junctions and size-varying capillaries in biological flows) and electric fields (in applications such as electroporation and dielectrophoresis). This work demonstrates biconcave-discoid to capped-cylindrical and prolate-spheroid shape transitions of a capsule in uniaxial extensional flow as well as in DC and AC electric fields. The shape changes of a stress-free biconcave-discoid capsule in external fields are important in determining the momentum and mass transfer between the capsule and the medium fluid as well as dielectrophoresis and electroporation phenomena of a capsule in an electric field. The biconcave-discoid to capped-cylindrical/prolate-spheroid shape transition is demonstrated for both a capsule (with parameters relevant to drug delivery) as well as for a red blood cell (physiological conditions). However, significant differences are observed in this shape transition depending upon the applied external fields. In an extensional flow, the pressure-driven transition shows the equator being squeezed in and the poles being pulled out to deform into a capped cylinder at low capillary number and a prolate spheroid at high capillary number. On the other hand, in the transition driven by electric fields, the shoulders of the capsule seem to play a significant role in the dynamics. The shape transition in the electric fields depends upon the relative magnitude of the electric and the hydrodynamic response times, particularly relevant for the dynamics of red blood cells in physiological conditions. A new method of analysing the shape transition of red blood cells in AC electric fields is suggested, where a large separation of time scales is observed between the hydrodynamic and electric responses.

Key words: boundary integral methods, capsule/cell dynamics, electrohydrodynamic effects

1. Introduction

The study of the interfacial rheological response of a red blood cell (RBC) membrane is of considerable significance given its relevance in biofluid dynamics and rheology. The membrane rheology of RBCs has been used to ascertain the health of biological cells in several studies using microfluidic devices (Lee *et al.* 2009*a*; Yaginuma *et al.* 2013; Henon, Sheard & Fouras 2014). An important

application of polymeric biconcave-discoid capsules (popular model of an RBC) is their use as promising drug-delivery carriers. In this context, it is of interest to understand the rheological behaviour as well as the response of a biconcave-discoid capsule to the deforming forces and the resulting dynamics (Kozlovskaya *et al.* 2014). Inspired by the shapes of the carriers in biological processes such as human RBCs as well as bio-organisms in nature such as bacteria (She *et al.* 2013, 2014), particles of varying shapes have been suggested for efficient drug delivery. Improved bio-functionality has been reported with hydrogel microparticles (Merkel *et al.* 2011) and capsules (Kozlovskaya *et al.* 2014) similar in size and shape to human RBCs. It is reported that the shape of the carrier/capsule is an important parameter in biological processes, influencing the enhanced cellular uptake of the loaded particle (Champion, Katare & Mitragotri 2007; Venkataraman *et al.* 2011). Ellipsoidal capsules have an ability to migrate laterally towards the wall of the vascular network in laminar flow, whereas RBCs preferably flow through the core (Lee, Ferrari & Decuzzi 2009*b*; Decuzzi *et al.* 2008).

From a mechanics point of view, RBCs can be considered to be comprised of a Newtonian suspension of haemoglobin dispersed in water and encapsulated by a lipid bilayer membrane and associated protein skeleton (spectrin network) (Evans 1980). The lipid bilayer has several embedded but mobile proteins which impart a complex rheology to the membrane. The RBC membrane incompressibility and interfacial viscous behaviour are attributed to the lipid bilayer and the proteins, respectively. The bilayer membrane is supported by a rigid protein (spectrin) network that endows an elastic behaviour (Mohandas & Evans 1994). This complex structure makes the cell membrane an area-preserving (incompressible) two-dimensional medium, and therefore, it resists change in the area by generating inhomogeneous but anisotropic tension. Moreover, unlike lipid bilayer membranes, which offer negligible resistance to shear, the RBCs offer minimal but significant resistance to shear deformation. Further, the resistance to bending (Pozrikidis 1990, 2003*a*; Kwak & Pozrikidis 2001) is significant in the regions of high curvature.

Pozrikidis (1990) studied the dynamics of RBCs in uniaxial extensional flow considering oblate-spheroid shapes. In this study, an initial oblate shaped cell was positioned axisymmetrically, and its dynamics was solved by the boundary integral method. Along with membrane elasticity, an area incompressibility constraint was employed, whereas the bending rigidity of the membrane was neglected. It was observed that oblate perturbed initial shapes evolved to prolate-spheroid shapes through different transitional shapes depending upon the reduced shear elasticity. In another analysis of the deformation of a spherical capsule in uniaxial extensional flow, Kwak & Pozrikidis (2001) reported that the bending rigidity of the membrane prevents the formation of sharp pointed tips at large deformation, and results in nearly cylindrical shapes with rounded caps.

An RBC develops a large membrane tension due to the area incompressibility constraint. Typically, a tension beyond 10 mN m^{-1} leads to the rupture of a membrane, resulting in haemolysis (Evans, Waugh & Melnik 1976). Despite this, it can admit a variety of shapes under deforming forces, due to a very low reduced volume. Although shear flow is commonly encountered in biological systems, the extensional flow profile often develops at the bifurcations of blood vessels and size-varying capillaries. Moreover, extensional flow provides an excellent framework to investigate soft particles, mainly due to its axisymmetric deformation field. The computational (Yen *et al.* 2015) and experimental (Lee *et al.* 2009*a*; Yen *et al.* 2015)

analyses suggested that the stress caused by the extensional flow plays a significant role in the haemolysis of an RBC as compared to the shear stress. Therefore, to understand the integrity of a synthetic biconcave-discoid capsule in maximum stress conditions encountered in applications, an analysis in extensional flow is essential.

An electric field can induce deformation (Chang, Takashima & Asakura 1985), change in orientation (Friend, Finch & Schwan 1975) and dielectrophoresis (Cruz & García-Diego 1998). It can also cause the fusion and lysis of biological cells (Scheurich *et al.* 1980). Engelhardt & Sackmann (1988) measured the shear elastic moduli of erythrocyte membranes by carrying out a deformation study in a high-frequency electric field (Engelhardt & Sackmann 1988). When the electric field was turned off, a highly elongated erythrocyte returned to the actual shape of the cell, thus supporting the proposed shape memory theory of an erythrocyte (Fischer 2004; Cordasco & Bagchi 2017). A reversible deformation was noticed at a low-intensity AC electric field, and the haemolysis of the cells was observed at a high-intensity field (Engelhardt & Sackmann 1988; Gass, Chernomordik & Margolis 1991; Krueger & Thom 1997). Moreover, the deformation also depends upon the conductivities of the inner and outer fluids (Sukhorukov, Mussauer & Zimmermann 1998; Kononenko & Shimkus 2000, 2002; Das & Thaokar 2018*b*). Apart from electrodeformation, electrorotation and its dependency on the conductivities of the fluids as well as the frequency of the applied AC electric field are observed (Das & Thaokar 2018*a*). Attempts have also been made to calculate Maxwell stresses at the interface of an erythrocyte (Sebastián *et al.* 2006). An improved understanding of the mechanics of RBCs has enabled the development of better medical diagnostic devices (Engelhardt & Sackmann 1988; Kononenko & Shimkus 2000; Kononenko 2002; Thom & Gollek 2006; Thom 2009; Du, Dao & Suresh 2014). A similar analysis can also be employed to measure the mechanical properties of the synthetic biconcave-discoid capsule.

Even though the change in shape and lysis of an RBC in an electric field were observed early on (Ur & Lushbaugh 1968), the underlying physics is still not well understood. Most of the studies considered erythrocytes as spheroidal (Chang *et al.* 1985; Ashe, Bogen & Takashima 1988; Joshi *et al.* 2002) or oblate (Pozrikidis 1990) shaped, although it is a biconcave discoid under normal quiescent conditions. Thus, it is important to carry out a consistent electrohydrodynamic analysis on the exact geometry of RBCs.

Knowledge of shape and shape transitions in biconcave discoids under external fields is important on three counts. First, the transport processes (mass, momentum, and heat) depend upon the instantaneous shape and shape changes under fields. Second, knowledge of the tension and tension distribution in these capsules depends upon a complicated coupling between shape and the external forces. Lastly, although a biconcave discoid could undergo a transition into a prolate spheroid, several questions can be raised. These include, what exactly is the mode of transition, is it a continuous or discontinuous transition? Would the pathways be similar or different, under different kinds of external forces such as extensional flow and electric fields? Would the final shapes, although expected to be axisymmetric but highly deformed spheroids, be similar or dependent upon the types of external forces?

It is known that extensional flows (Diaz, Pelekasis & Barthès-Biesel 2000; De Loubens *et al.* 2015) and uniform electric fields (Karyappa, Deshmukh & Thaokar 2014; Das & Thaokar 2018*b*) cause identical deformations in spherical capsules, owing to the similar angular distribution of the stresses (electric and hydrodynamic) at the capsule interface. Our study confirms that these two different force fields cause similar deformations in RBCs as well. It is then of interest to understand these two

force fields with respect to their similar and dissimilar characteristics, as well as their relative merits in possible experiments.

Based on the above discussion of the literature, the following key objectives are the motivation for the present study: (i) to understand the dynamics of a biconcave discoid under axisymmetric external fields, such as extensional flow and uniform electric fields, and explore the possibility of a biconcave-discoid to prolate-spheroid transition in physiological and typical experimental conditions; (ii) to determine the pathways of such a transition and the differences in the pathways when extensional flow or electric fields are used; (iii) to examine the differences between the responses to AC and DC fields, as well as the effect of the ratio of the electric to hydrodynamic time scale on the transition and the associated shapes; (iv) to determine the mechanism of the dynamics by a detailed analysis of hydrodynamic, electric, and elastic stress distributions; (v) to obtain transmembrane potential distribution in biconcave discoids, which has relevance in electroporation studies. Although few experimental studies have been reported for near-RBC-shaped microcapsules, they lack a theoretical analysis to comprehend their rheological behaviour. This is essentially due to their complicated shapes, which make it difficult to obtain closed-form analytical solutions. In this analysis, the transient deformation is computed numerically using the boundary integral method for Stokes flow and considering the Skalak law as the model for the elastic membrane.

2. Boundary integral formulations

The axisymmetric deformation of a biconcave-discoid elastic capsule and RBC (commonly called as capsule in this article) under a uniaxial extensional flow at vanishing Reynolds number is investigated. In the Cartesian coordinate system, axisymmetric extensional flow is given by

$$\tilde{\boldsymbol{u}}^{\infty} = e \begin{bmatrix} -1 & 0 & 0 \\ 0 & 2 & 0 \\ 0 & 0 & -1 \end{bmatrix} \tilde{\boldsymbol{x}}, \tag{2.1}$$

where e is the axisymmetric uniaxial extensional strain rate and $\tilde{\boldsymbol{x}}$ is the position vector. The position vector is given by $\tilde{\boldsymbol{x}} = \tilde{x}\boldsymbol{e}_x + \tilde{y}\boldsymbol{e}_y + \tilde{z}\boldsymbol{e}_z$, where $\boldsymbol{e}_x$, $\boldsymbol{e}_y$ and $\boldsymbol{e}_z$ are the unit vectors in the x, y and z-directions, respectively. The axis of symmetry of the capsule is assumed to coincide with the y-axis, such that its centroid is at the origin (see figure 1d). In this article, all the notations with and without a tilde (˜) represent dimensional and their non-dimensional counterparts, respectively.

The shape of a capsule is considered as that of a healthy human RBC (erythrocyte). Although the RBCs have been modelled as oblate spheroids (Pozrikidis 1990), there is a significant difference between the shape of a biconcave discoid and an oblate spheroid. Figure 1(c) shows that the oblate-spheroid shapes considered by Pozrikidis (1990) are quite different from the commonly conceived biconcave-discoid shape of a healthy human RBC. Equation (2.2) describes the shape of an RBC possessing a biconcave-discoid shape under normal physiological conditions (Evans & Fung 1972):

$$\tilde{y} = \pm a\frac{\alpha}{2}\left(1 - \frac{\tilde{r}^{\,2}}{\alpha^2}\right)^{1/2}\left(0.207161 + 2.002558\frac{\tilde{r}^{\,2}}{\alpha^2} - 1.122762\frac{\tilde{r}^{\,4}}{\alpha^4}\right), \tag{2.2}$$

where $\alpha = 1.385818$ is the ratio of the maximum radius of the biconcave discoid in the transverse plane of symmetry and equivalent radius a, the radius of a sphere of
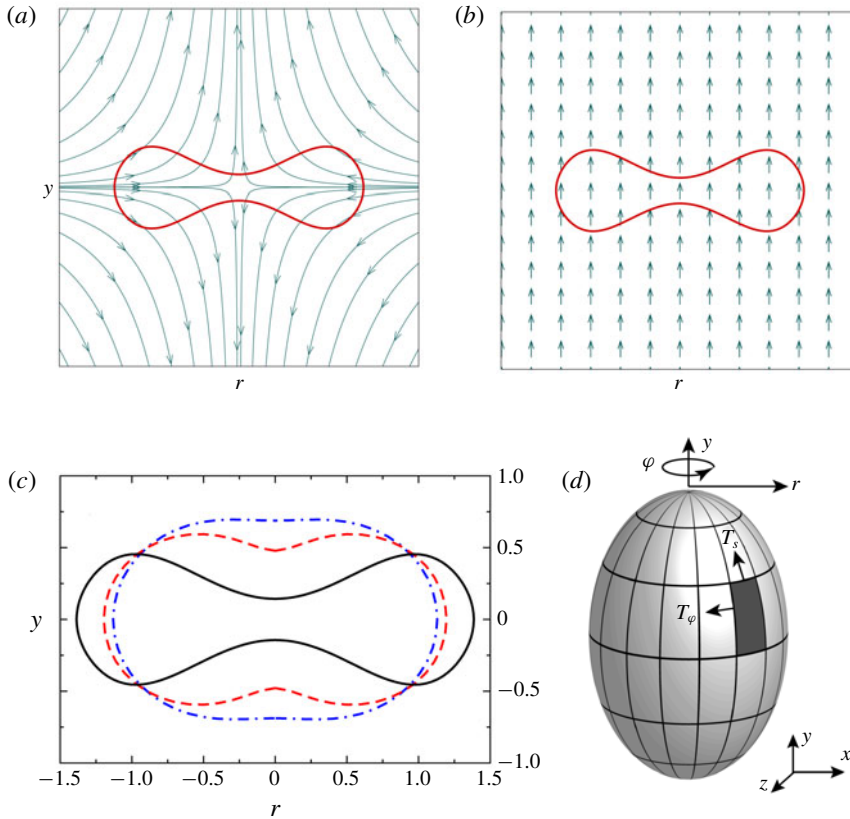
FIGURE 1. (Colour online) Schematic representation of a capsule in (*a*) extensional flow (curves with arrows represent streamlines) and (*b*) uniform electric field (arrows represent field lines). (*c*) Comparison of the shape of an RBC (——) with the oblate spheroids perturbed with a second-degree Legendre mode (—— for $\epsilon = -0.5$ and — · — for $\epsilon = -0.3$). (*d*) Schematic presentation of a prolate spheroid representing azimuthal (T_ϕ) and meridional (T_s) elastic tensions. The centre of the spheroid is at the origin of the Cartesian coordinate system.

equal volume. Here, $\tilde{y}$ and $\tilde{r} = \sqrt{\tilde{x}^2 + \tilde{z}^2}$ are the surface coordinates of the RBC in the cylindrical coordinate system, where $\tilde{r}$ defines the radial coordinate. The thickness of the RBC membrane is $\sim$10 nm, which is much smaller than the RBC's equatorial diameter ($\sim$8 µm) (Helfrich & Deuling 1975).

Both the outer and the inner fluids are Newtonian, and the viscosities of the outer and inner fluids are denoted by μ_e and $\lambda\mu_e$, respectively, where λ is the viscosity ratio. The mechanical properties of the membrane are the surface Young modulus, E_s (force/length), and bending rigidity, κ_b. The membrane of the capsule is considered to be purely elastic, and its viscous resistance is neglected. In the analysis of deformation in extensional flow and electric fields, the length is scaled by a, the equivalent radius of the capsule. For the analysis under extensional flow, the time, fluid velocity, stress (force/area), pressure and tensions are scaled by $\mu_e a/E_s$, E_s/μ_e, E_s/a, E_s/a and E_s, respectively.

We also describe an investigation on the axisymmetric deformation of a biconcave-discoid capsule subjected to a uniform DC electric field represented by $\tilde{\boldsymbol{E}}_{DC}^\infty = \tilde{E}_0^{DC}\boldsymbol{e}_y$,

where $\tilde{E}_0^{DC}$ is the electric field strength. Moreover, we investigate the electrohydrodynamic response of an RBC in an AC electric field, $\tilde{\boldsymbol{E}}_{AC}^\infty = \tilde{E}_0^{AC} \cos(\tilde{\omega}\tilde{t})\boldsymbol{e}_y$. Here, $\tilde{E}_0^{AC}$ and $\tilde{\omega}$ are the amplitude and frequency of the applied electric field, respectively, and $\tilde{t}$ is the time.

For the inner and outer fluid media, the dielectric constants and electrical conductivities are $\epsilon_{i,e}$ and $\sigma_{i,e}$, respectively. Subscripts i and e identify parameters for inner and the outer fluids, respectively. The ratio of conductivities of the inner and outer fluids is denoted by $\sigma_r = \sigma_i/\sigma_e$, and the ratio of dielectric constants is denoted by $\epsilon_r = \epsilon_i/\epsilon_e$. The electrical properties of the capsule membrane are the capacitance, C_m, and the conductance, G_m. In the analysis of the dynamics of a biconcave-discoid capsule in the DC electric field, the scaling is motivated by the electrostatics model and is discussed later.

For simplicity of computations, the interface is considered to be impermeable to the fluids over the simulation time scale, thereby preventing flow across the membrane. The effect of bending is also considered in the present analysis, which was ignored in earlier work by Zhou & Pozrikidis (1995). The ratio of the elastic to the bending force is given by $(\Delta X/h^2 L)/4H^2$, where h is the thickness of the membrane, L is the typical size, and ΔX is the deformation. The bending force can be neglected only if the mean curvature $H < 1/2\sqrt{\Delta X/h^2 L}$.

For the boundary integral simulation, the parameters considered for the biconcave-discoid capsule (Pozrikidis 2005; Karyappa *et al.* 2014) and the human RBC in physiological conditions (Beving *et al.* 1994; Haidekker *et al.* 2002; Pozrikidis 2003*b*; Wolf *et al.* 2011; Freund 2014; Secomb 2017) are shown in table 1.

All the non-hydrodynamic and hydrodynamic forces responsible for the deformation of a biconcave-discoid capsule and RBC are discussed in the following sections.

2.1. *Elastic forces*

The interface of a capsule is considered to be thin and elastic, as described by the Skalak model (Skalak *et al.* 1973). According to the Skalak law, the non-dimensional membrane elastic tension in the principal direction i (where i can be s or ϕ, see figure 1*d*) is expressed as a function of the principal stretch ratios ($\lambda_{i,j}$) for a strain hardening membrane as

$$\tilde{T}_i^{SK} = \frac{G^{SK}}{\lambda_i \lambda_j}[\lambda_i^2(\lambda_i^2 - 1) + C(\lambda_i \lambda_j)^2\{(\lambda_i \lambda_j)^2 - 1\}]. \tag{2.3}$$

Membrane tension in the principal direction j can be expressed by interchanging indices in the constitutive relation (2.3). In this work, i is the meridional and j is the azimuthal principal direction, and the corresponding tensions are considered as T_s and T_ϕ. The principal stretch ratios are defined as $\lambda_s = d\tilde{s}/d\tilde{S}$ and $\lambda_\phi = \tilde{r}/\tilde{R}$, where s and r are the measures of arclength and the radius of the deformed capsule, and the upper case alphabets represent their counterparts in the stress-free shape, respectively. The first and second terms on the right-hand side of equation (2.3) are the measures of the shear deformation associated with the modulus G^{SK} and the area dilatation with the modulus CG^{SK}, respectively (Skalak *et al.* 1973). The area dilatation parameter C regulates the extent of change of surface area; a large value of C restricts the membrane dilatation. In the small deformation limit, G^{SK} is related to the surface Young modulus, E_s (Barthès-Biesel, Diaz & Dhenin 2002) as $E_s = 2G^{SK}(1 + 2C)/(1 + C)$.

Parameters	Capsule ($C = 1$ and 10)	RBC ($C = 1$ and 10)	Scaled variables	Magnitude of scaled variables
a (μm)	5	2.82^a	—	—
E_s (N m^{-1})	0.1	6.1×10^{-6}	—	—
κ_b (N m)	2.5×10^{-15}	2×10^{-19}	$\hat{\kappa}_b$	0.001
μ_e (mPa s at 21 °C)	100	1.6	—	—
μ_i (mPa s at 21 °C)	100	8.0	λ	1^b
ϵ_e	80	70	—	—
ϵ_i	80	42	ϵ_r	1 (Capsule) 0.6 (RBC)
σ_e (S m^{-1})	10^{-4}	0.74	—	1
σ_i (S m^{-1})	10^{-3} and 10^{-5}	0.78	σ_r	0.1, 10 (Capsule) 1.054 (RBC)
C_m (F m^{-2})	0.01	0.035	$\hat{C}_m$	50 (Capsule) 282 (RBC)
G_m (S m^{-2})	0	0.1	$\hat{G}_m$	0
$\tilde{t}_e$ (s)	7.2×10^{-6}	0.837×10^{-9}	t_e	1 (Capsule) 3.5×10^{-3} (RBC)
$\tilde{t}_H$ (s)	5.0×10^{-6}	1.3×10^{-3}	t_H	1 (Capsule) 1 (RBC)
$\tilde{t}_{MW}$ (s)	2.0×10^{-6} ($\sigma_r = 10$) 1.01×10^{-5} ($\sigma_r = 0.1$)	0.713×10^{-9}	t_{MW}	0.28 ($\sigma_r = 10$), 1.403 ($\sigma_r = 0.1$) (Capsule) 3.0×10^{-3} (RBC)
$\tilde{t}_{cap}$ (s)	3.0×10^{-4} ($\sigma_r = 10$) 5.25×10^{-3} ($\sigma_r = 0.1$)	3.42×10^{-7}	t_{cap}	41.67 ($\sigma_r = 10$), 729.2 ($\sigma_r = 0.1$) (Capsule) 1.45 (RBC)

TABLE 1. Values of parameters and scaled variables used in boundary integral simulation for the biconcave-discoid capsule and human RBC.

^{a}The equivalent radius of a capsule is considered in estimating scaled parameters.
^{b}For RBC $\lambda \sim 5$ in physiological condition.

The membrane elastic traction (force/area), governed by the combined contribution of the elastic tensions (force/length) obtained from the constitutive law, is given by $\Delta \boldsymbol{f}^{el} = \tau_n^{el} \boldsymbol{n} + \tau_t^{el} \boldsymbol{t}$. The components of the elastic stresses can be obtained as

$$\tau_n^{el} = -(K_s T_s + K_\phi T_\phi), \tag{2.4a}$$

$$\tau_t^{el} = \frac{\mathrm{d}T_s}{\mathrm{d}s} + \frac{1}{r}\frac{\mathrm{d}r}{\mathrm{d}s}(T_s - T_\phi), \tag{2.4b}$$

where $K_s = |\mathrm{d}\boldsymbol{t}/\mathrm{d}s|$ and $K_\phi = n_r/r$ are the curvatures of the meridional surface in the principal directions s and ϕ, respectively. The components of the unit normal and the tangent vectors at the interface can be calculated as $t_y = n_r = \mathrm{d}y/\mathrm{d}s$ and $t_r = -n_y = \mathrm{d}r/\mathrm{d}s$.

2.2. Resistance to bending

Even though a thin elastic membrane offers negligible resistance to bending, it can have a significant contribution to the restoring forces, especially in the regions of high

curvature. The overall non-dimensional bending force (force/area) is given by

$$\Delta \boldsymbol{f}^b = \hat{\kappa}_b [2\Delta_s H + (2H - c_0)(2H^2 - 2K_G + c_0 H)]\boldsymbol{n}, \tag{2.5}$$

where $\hat{\kappa}_b = \kappa_b/a^2 E_s$ is the non-dimensional bending rigidity, $H = (k_s + k_\phi)/2$ is the mean curvature, $K_G = k_s k_\phi$ is the Gaussian curvature, and c_0 is the spontaneous curvature (Vlahovska, Podgorski & Misbah 2009; Yazdani, Kalluri & Bagchi 2011). In the axisymmetric cylindrical coordinate system, the Laplace–Beltrami of the mean curvature is given as (Hu, Kim & Lai 2014)

$$\Delta_s H = \boldsymbol{\nabla}_s \cdot (\boldsymbol{\nabla}_s H) = \frac{1}{r|\boldsymbol{x}_s|} \frac{\partial}{\partial s} \left(\frac{r}{|\boldsymbol{x}_s|} \frac{\partial H}{\partial s} \right), \tag{2.6}$$

where $|\boldsymbol{x}_s| = \sqrt{(\partial r/\partial s)^2 + (\partial y/\partial s)^2}$. A spectral method is used to calculate the higher-order derivatives of mean curvature with respect to the arclength, especially for improved accuracy in estimating the bending force (Trefethen 1996). For the boundary integral analyses of the deformation of a capsule and RBC in both the extensional flow and electric field, a fixed value of $\hat{\kappa}_b = 0.001$ is considered (Freund 2014; Guckenberger & Gekle 2017).

2.3. *Electrostatics*

For the analysis of the dynamics of deformation of a biconcave-discoid capsule in an externally applied DC electric field, the charge relaxation time of the outer fluid, $\tilde{t}_e = \epsilon_e \epsilon_0 / \sigma_e$, is considered as the scaling for time, where ϵ_0 is the permittivity of the free space. The bulk fluids are assumed to be electroneutral on account of $\kappa^{-1} \ll a$, where κ^{-1} is the Debye screening length. Other time scales of relevance are the hydrodynamic response time, $\tilde{t}_H = \mu_e a / E_s$, the Maxwell–Wagner relaxation time, $\tilde{t}_{MW} = \epsilon_0(\epsilon_i + 2\epsilon_e)/(\sigma_i + 2\sigma_e)$, and the membrane charging time, $\tilde{t}_{cap} = aC_m(1/\sigma_i + 1/2\sigma_e)$. The non-dimensional counterparts of these time scales are $t_e = 1$, $t_H = \tilde{t}_H/\tilde{t}_e$, $t_{MW} = \tilde{t}_{MW}/\tilde{t}_e = (2 + \epsilon_r)/(2 + \sigma_r)$ and $t_{cap} = \tilde{t}_{cap}/\tilde{t}_e = \hat{C}_m(1/2 + 1/\sigma_r)$ (Grosse & Schwan 1992). Fluid velocity ($\tilde{\boldsymbol{u}}$), electric field ($\tilde{\boldsymbol{E}}$), potential ($\tilde{V}$), and stress are scaled by E_s/μ_e, E_0, $E_0 a$ and E_s/a, respectively.

The electric potential inside and outside the biconcave-discoid capsule satisfies the Laplace equation, $\nabla^2 V_{i,e} = 0$. The electric potential can be obtained by solving the Laplace equation and using Green's theorem as

$$\frac{1}{2}V_i(\boldsymbol{x}_0) = \int_s [G^E(\boldsymbol{x}, \boldsymbol{x}_0)\boldsymbol{\nabla} V_i(\boldsymbol{x}) \cdot \boldsymbol{n}(\boldsymbol{x}) - V_i(\boldsymbol{x})\boldsymbol{n}(\boldsymbol{x}) \cdot \boldsymbol{\nabla} G^E(\boldsymbol{x}, \boldsymbol{x}_0)] \,\mathrm{d}s(\boldsymbol{x}), \tag{2.7a}$$

$$\frac{1}{2}V_e(\boldsymbol{x}_0) = V^\infty(\boldsymbol{x}_0)$$
$$- \int_s [G^E(\boldsymbol{x}, \boldsymbol{x}_0)\boldsymbol{\nabla} V_e(\boldsymbol{x}) \cdot \boldsymbol{n}(\boldsymbol{x}) - V_e(\boldsymbol{x})\boldsymbol{n}(\boldsymbol{x}) \cdot \boldsymbol{\nabla} G^E(\boldsymbol{x}, \boldsymbol{x}_0)] \,\mathrm{d}s(\boldsymbol{x}), \tag{2.7b}$$

where $G^E(\boldsymbol{x}, \boldsymbol{x}_0) = 1/4\pi|\hat{\boldsymbol{x}}|$ is the Green function for the Laplace equation (McConnell, Vlahovska & Miksis 2015). $\hat{\boldsymbol{x}} = \boldsymbol{x} - \boldsymbol{x}_0$, where $\boldsymbol{x}_0$ and $\boldsymbol{x}$ are the source and observation points, respectively.

The discontinuity in electrical potential at the interface is termed as the transmembrane potential ($V_m = V_i - V_e$), and it can be calculated by solving (2.7a) and (2.7b) along with electrical current continuity across the membrane:

$$\sigma_r E_{n,i} + \epsilon_r \frac{\mathrm{d}E_{n,i}}{\mathrm{d}t} = E_{n,e} + \frac{\mathrm{d}E_{n,e}}{\mathrm{d}t} = \hat{C}_m \frac{\mathrm{d}V_m}{\mathrm{d}t} + \hat{G}_m V_m, \tag{2.8}$$

where $E_{n,i,e}$ are normal electric fields inside and outside of the membrane. The current in the fluids is assumed to be Ohmic and displacement currents corresponding to the Ohmic resistance and the capacitance in the bulk to be in a parallel circuit. In this model, the thickness of the double layer is infinitesimally thin such that the interfacial free charge is given by $E_{n,e} - \epsilon_r E_{n,i} = q$, where q is the non-dimensional charge density. The non-dimensional capacitance and conductance of the membrane are $\hat{C}_m = aC_m/\epsilon_e\epsilon_0$ and $\hat{G}_m = aG_m/\sigma_e$.

The Maxwell electric stress tensor in a fluid is defined as $\tilde{\boldsymbol{\tau}}^E = \epsilon\epsilon_0(\tilde{\boldsymbol{E}}\tilde{\boldsymbol{E}} - (1/2)\tilde{E}^2\boldsymbol{I})$, where $\boldsymbol{I}$ is the identity tensor. The net non-dimensional electric traction at the interface is given by $\Delta\boldsymbol{f}^E = \boldsymbol{n} \cdot (\boldsymbol{\tau}_e^E - \boldsymbol{\tau}_i^E) = \tau_n^E\boldsymbol{n} + \tau_t^E\boldsymbol{t}$, where the components of electric stresses are

$$\tau_n^E = \tfrac{1}{2}[(E_{n,e}^2 - E_{t,e}^2) - \epsilon_r(E_{n,i}^2 - E_{t,i}^2)], \tag{2.9a}$$

$$\tau_t^E = E_{n,e}E_{t,e} - \epsilon_r E_{n,i}E_{t,i}. \tag{2.9b}$$

2.4. *Hydrodynamics*

From the values of parameters in table 1, the particle Reynolds number is $Re_p \sim 10^{-2}$; therefore the flow inside and outside of the capsule can be described by the Stokes equations (Secomb 2017)

$$\boldsymbol{\nabla} \cdot \boldsymbol{u} = 0, \quad \boldsymbol{\nabla} \cdot \boldsymbol{\tau}^H = 0, \tag{2.10}$$

where $\boldsymbol{u}$ is the fluid velocity and $\boldsymbol{\tau}^H$ is the viscous stress. Viscous stresses for the inner and outer fluid media are given by

$$\boldsymbol{\tau}_i^H = -P\boldsymbol{I} + \lambda(\boldsymbol{\nabla}\boldsymbol{u} + \boldsymbol{\nabla}\boldsymbol{u}^{\mathrm{T}}), \tag{2.11a}$$

$$\boldsymbol{\tau}_e^H = -P\boldsymbol{I} + (\boldsymbol{\nabla}\boldsymbol{u} + \boldsymbol{\nabla}\boldsymbol{u}^{\mathrm{T}}), \tag{2.11b}$$

respectively, where P is the fluid pressure.

Far from the capsule membrane ($|\boldsymbol{x}| \to \infty$), $\boldsymbol{u} \to \boldsymbol{u}^\infty$, where $\boldsymbol{u}^\infty$ is assumed to be the undistorted flow velocity of the outer fluid and is given by the dimensional form of the applied velocity in (2.1). The solution of the above equations gives rise to an integral equation for the interfacial velocity Rallison & Acrivos (1978) in a non-dimensional form as

$$\boldsymbol{u}(\boldsymbol{x}_0) = \frac{2}{1+\lambda}\boldsymbol{u}^\infty(\boldsymbol{x}_0) - \frac{1}{1+\lambda}\frac{1}{4\pi}\int_s \Delta\boldsymbol{f}(\boldsymbol{x}) \cdot \boldsymbol{G}(\boldsymbol{x}, \boldsymbol{x}_0)\,\mathrm{d}s(\boldsymbol{x})$$
$$+ \frac{1}{4\pi}\frac{1-\lambda}{1+\lambda}\int_s \boldsymbol{u}(\boldsymbol{x}) \cdot \boldsymbol{Q}(\boldsymbol{x}, \boldsymbol{x}_0) \cdot \boldsymbol{n}(\boldsymbol{x})\,\mathrm{d}s(\boldsymbol{x}), \tag{2.12}$$

where $\boldsymbol{G}(\boldsymbol{x}, \boldsymbol{x}_0)$ and $\boldsymbol{Q}(\boldsymbol{x}, \boldsymbol{x}_0)$ are Green's functions for velocity and stress, respectively, and $\Delta\boldsymbol{f}$ is the unbalanced non-hydrodynamic traction at the interface. For an unbounded three-dimensional flow, explicit expressions for these tensors are

$$\boldsymbol{G}(\boldsymbol{x}, \boldsymbol{x}_0) = \frac{\boldsymbol{I}}{|\hat{\boldsymbol{x}}|} + \frac{\hat{\boldsymbol{x}}\hat{\boldsymbol{x}}}{|\hat{\boldsymbol{x}}|^3}, \quad \boldsymbol{Q}(\boldsymbol{x}, \boldsymbol{x}_0) = -6\frac{\hat{\boldsymbol{x}}\hat{\boldsymbol{x}}\hat{\boldsymbol{x}}}{|\hat{\boldsymbol{x}}|^5}. \tag{2.13a,b}$$

The general boundary integral equation (2.12) is solved for the velocity of the interface of an axisymmetric deformable capsule in an axisymmetric flow and applied

electric field. For the analysis of the dynamics of a biconcave-discoid capsule and an RBC subjected to a uniform electric field, the stagnant outer fluid medium is considered; therefore $\boldsymbol{u}^\infty = 0$.

Finally, the shape evolves to $\boldsymbol{x}(t + \Delta t)$ with the kinematic condition given by

$$\boldsymbol{x}(t + \Delta t) = \boldsymbol{x}(t) + k_f \boldsymbol{u}(\boldsymbol{x}) \Delta t, \tag{2.14}$$

where $\boldsymbol{x}(t)$ is the shape of the capsule at the current time, t, and Δt is the time step considered for the boundary integral simulation. In (2.14), the kinematic factor k_f depends upon the scaling of the variables, and is described in the corresponding sections.

2.5. *Pressure calculation*

The inside and outside pressure of a capsule can be calculated using the boundary integral equations, given as

$$
\begin{aligned}
P_i(\boldsymbol{x}_0) &= -\frac{1}{8\pi} \int_s \Delta \boldsymbol{f}(\boldsymbol{x}) \cdot \boldsymbol{p}(\boldsymbol{x}, \boldsymbol{x}_0) \, \mathrm{d}S(\boldsymbol{x}) \\
&\quad + \lambda \frac{1-\lambda}{8\pi} \int_s \boldsymbol{u}(\boldsymbol{x}) \cdot \boldsymbol{\Pi}(\boldsymbol{x}, \boldsymbol{x}_0) \cdot \boldsymbol{n}(\boldsymbol{x}) \, \mathrm{d}S(\boldsymbol{x}),
\end{aligned} \tag{2.15a}
$$

$$
\begin{aligned}
P_e(\boldsymbol{x}_0) &= -\frac{1}{8\pi} \int_s \Delta \boldsymbol{f}(\boldsymbol{x}) \cdot \boldsymbol{p}(\boldsymbol{x}, \boldsymbol{x}_0) \, \mathrm{d}S(\boldsymbol{x}) \\
&\quad + \frac{1-\lambda}{8\pi} \int_s \boldsymbol{u}(\boldsymbol{x}) \cdot \boldsymbol{\Pi}(\boldsymbol{x}, \boldsymbol{x}_0) \cdot \boldsymbol{n}(\boldsymbol{x}) \, \mathrm{d}S(\boldsymbol{x}),
\end{aligned} \tag{2.15b}
$$

where $\boldsymbol{p}(\boldsymbol{x}, \boldsymbol{x}_0)$ and $\boldsymbol{\Pi}(\boldsymbol{x}, \boldsymbol{x}_0)$ are the free space Green's functions for pressure (Pozrikidis 1992; Lac, Morel & Barthès-Biesel 2007).

$$\boldsymbol{p}(\boldsymbol{x}, \boldsymbol{x}_0) = 2\frac{\hat{\boldsymbol{x}}}{\hat{\boldsymbol{x}}^3}, \quad \boldsymbol{\Pi}(\boldsymbol{x}, \boldsymbol{x}_0) = 4 \left(-\frac{\boldsymbol{I}}{|\hat{\boldsymbol{x}}|^3} + 3\frac{\hat{\boldsymbol{x}}\hat{\boldsymbol{x}}}{|\hat{\boldsymbol{x}}|^5} \right). \tag{2.16a,b}$$

3. Results and discussion

3.1. *Dynamics of a capsule in extensional flow*

The scaling of (2.1) gives rise to a non-dimensional quantity $Ca_f = \mu ea/E_s$, which is termed as the flow capillary number and determines the dynamics of the deformation of a capsule. The hydrodynamic force at the interface is balanced by the elastic and bending forces, i.e. $\Delta \boldsymbol{f}^H = -(\Delta \boldsymbol{f}^{el} + \Delta \boldsymbol{f}^b)$. With the values of the parameters in table 1 for the simulation of a biconcave-discoid capsule in extensional flow, the kinematic factor $k_f = 1$. The Skalak membrane parameter C is assumed to be 1 and 10 for two separate studies.

The analysis of the dynamics of deformation of a capsule in extensional flow is presented for a small dilatation parameter ($C = 1$ in this case). It is observed that a considerable change in area ($\sim 13\%$) is admitted when the capsule is subjected to a strong extensional flow. The capillary numbers are chosen in such a way that they demonstrate three possible modes of deformation. Figure 2(*a–c*) shows that at a small value of destabilizing force ($Ca_f = 0.015$), the deformation is small and
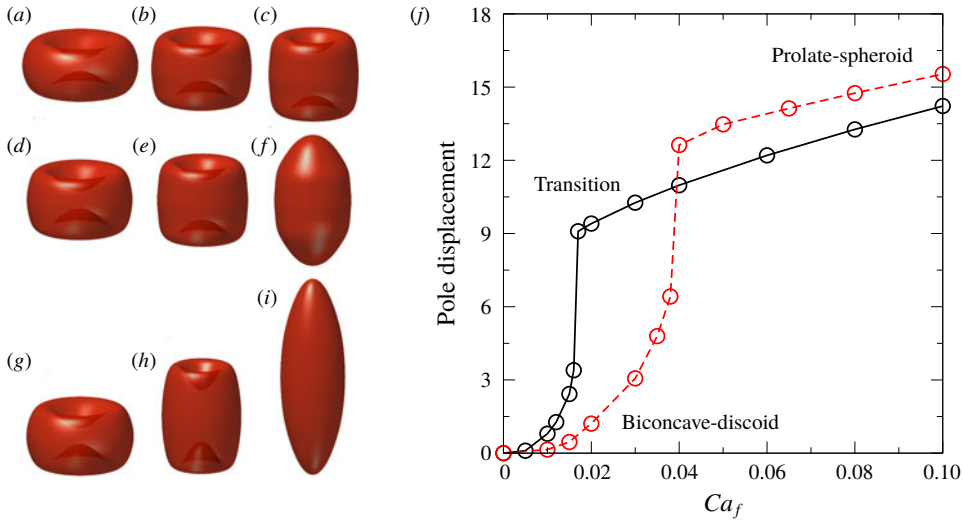
FIGURE 2. (Colour online) Observed shapes during the evolution of a capsule at (*a*) $t = 10$, (*b*) $t = 40$, (*c*) $t = \infty$ for $Ca_f = 0.015$; (*d*) $t = 20$, (*e*) $t = 70$ (*f*) $t = \infty$ for $Ca_f = 0.017$; and (*g*) $t = 2$, (*h*) $t = 7$, (*i*) $t = \infty$ for $Ca_f = 0.1$, considering the dilatation parameter $C = 1$. (*j*) Equilibrium displacement of the north pole from the initial position of an undeformed biconcave-discoid as a function of Ca_f for $C = 1$ (———) and $C = 10$ (— —).

the biconcavity is maintained. The capsule slowly deforms such that the concavities at the poles are affected the most (see figure 2*a*,*b*); subsequently, the flow reduces the depression (in a way opening them up) and eventually reaches a steady-state biconcave-cylindrical shape, as shown in figure 2(*c*). A capsule does not open up into a prolate spheroid until a threshold capillary number is reached (in this case, $Ca_f = 0.017$). At such a threshold capillary number ($Ca_f = 0.017$) the capsule shows a remarkable shape transition wherein the biconcave cavities (see figure 2*d*,*e*) open up and transform into a steady capped-cylindrical shape (a cylindrical body with convex caps at both ends) (see figure 2*f*). At a still higher capillary number ($Ca_f = 0.1$), the dynamics is faster, and very similar behaviour is observed (see figure 2*g*–*i*), and the capsule attains a highly stretched prolate-spheroid shape (see figure 2*i*).

Figure 2(*j*) represents the equilibrium displacement of the north pole (($y_p - y_{p0})/y_{p0}$, where y_p and y_{p0} are the positions of the pole in the deformed and undeformed states, respectively) from its position in the undeformed shape as a function of capillary number. Figure 2(*j*) suggests that the evolution of the biconcave discoid to the capped cylindrical and prolate spheroid undergoes a discontinuous shape transition at the critical capillary number, i.e. $Ca_f = 0.017$ for $C = 1$ and $Ca_f = 0.04$ for $C = 10$. For the deformation of a Skalak capsule, a large dilatation parameter restricts the change in surface area, although at the cost of numerical stiffness. Therefore, the analysis is restricted to a maximum value of dilatation parameter $C = 10$ allowing ∼10 % change in surface area. The higher threshold value ($Ca_f = 0.04$ compared to $Ca_f = 0.017$ at $C = 1$) of the capillary number at $C = 10$ suggests the greater extent of the membrane resistance to the deformation that leads to a biconcave-discoid to capped-cylindrical transition as well as a prolate-spheroid shape transition.

To understand the mechanism for the transition from a biconcave shape to a prolate spheroid, the pressure profile and elastic tension over the half arclength are plotted
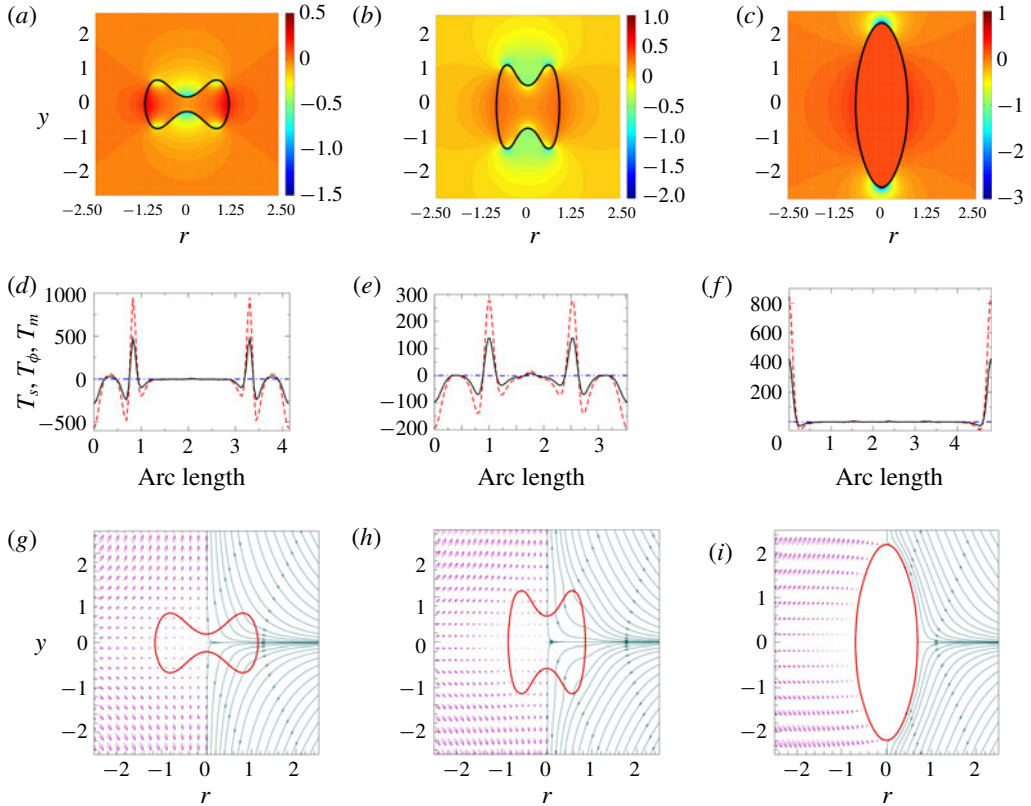
FIGURE 3. (Colour online) At $Ca_f = 0.1$ and $C = 1$. (a–c) Pressure profile. (d–f) Variation of the meridional, T_s (——), azimuthal, T_ϕ (— · —) and mean, T_m (——) elastic tensions along the arclength. (g–i) Streamlines (shown only in the right-hand half) and the velocity profile (relative magnitude of the flow is proportional to the length of the short arrows shown in the left-hand half). From left to right the columns correspond to times $t = 2, 7$ and ∞, respectively.

in figure 3(a–c) and figure 3(d–f), respectively. The applied free stream uniaxial extensional flow does not have an associated pressure profile because the velocity is linear. When a rigid spherical particle is placed in such a flow, it generates a velocity field to bring the velocity of the applied flow to zero on the particle surface. This generates stress on the particle from the equator to the poles, which the particle transmits to the fluid (from poles to equator), thereby leading to a stresslet-induced disturbance velocity field. Since, in the case of a rigid spherical particle, the particle brings the fluid to rest at its surface, the fluid has to generate a positive pressure at the equator to resist the incoming flow and a negative pressure at the poles to suck fluid into the poles. When the surface/interface is not rigid (e.g. a drop), it can give way under this pressure and build a curvature. In a drop, this can result in a dimple at the equator and a bump at the pole (the drop will try to adjust its curvature to satisfy the Young–Laplace equation at the interface) leading to a prolate-spheroid shape. Similar arguments will mean that the shape of a drop will be oblate in biaxial extensional flow.

In a capsule, the meridional and azimuthal tensions could be anisotropic and compressive, unlike the isotropic tension in a liquid–liquid interface (a drop). While a spherical drop cannot maintain its shape in extensional flow, a capsule can maintain a near-spherical shape by generating a pressure inside which is intermediate between that at the equator and the poles on the outer side. This can be attained by a compressive membrane tension (predominantly azimuthal) at the equator and a tensile membrane tension at the poles. In the case of a biconcave-discoid capsule, a similar distribution of membrane tension (compressive at the equator and tensile at the poles) can support an extensional flow, except the pressure inside is now less than that at the poles.

When the capillary number is increased beyond the threshold, at short times ($t = 2$), the pressure is lower at the poles, thereby generating an internal flow from the equator to the poles. This leads to the shoulders of the biconcave-discoid capsule opening up. The pressure generated at the equator is so high that the resulting inside pressure at the poles continues to drive the fluid to the poles ($t = 7$). This fluid flow (see figure 3g–i) eventually leads to the opening up of the poles and transformation of the biconcave-discoid shape into a prolate spheroid (see figure 2i).

The elastic tensions are predominantly compressive, except at the shoulders. At the poles, as the curvature is negative and the inside pressure is higher than at outside (see figure 3a,b), the stresses have to be compressive (see figure 3d,e). The tension at the shoulders, however, is tensile, leading to a higher pressure inside the capsule, which further assists the shoulders to disappear by pushing the fluid into the poles.

For the deformed prolate spheroid at the steady state, the inside pressure is uniform at the equator (see figure 3c); therefore, the flow inside disappears (see figure 3i). The pressure inside is nearly identical to the outside pressure, due to the small curvature at the equator. Thereby, the mean elastic tension at the equator disappears (see figure 3f). At the poles, the outside pressure is lower compared to the inside pressure (see figure 3c), and since the curvature is positive, a high tensile mean elastic tension (see figure 3f) is generated.

3.2. *Dynamics of a biconcave-discoid capsule in DC electric fields*

The analysis of deformation of an elastic biconcave-discoid capsule in DC electric fields is carried out in the absence of free stream fluid velocity, $\boldsymbol{u}^\infty = 0$. Therefore, the hydrodynamic traction is balanced by the elastic traction, electric traction, and the traction due to bending rigidity, i.e.

$$\Delta \boldsymbol{f}^H = -(\Delta \boldsymbol{f}^{el} + Ca_e \Delta \boldsymbol{f}^E + \hat{\kappa}_b \Delta \boldsymbol{f}^b), \tag{3.1}$$

where $Ca_e = \epsilon_e \epsilon_0 a E_0^2 / E_s$ is the electric capillary number. The scaling of variables results in the kinematic factor as the hydrodynamic response time, i.e. $k_f = 1/t_H$. Considering the parameters in table 1, $E_s \sim 0.1$ N m^{-1}, $\mu_e \sim 0.1$ Pa s, $\sigma_e \sim 0.1$ mS m^{-1} and $\epsilon_e \sim 80$, for the dynamics of a capsule with an equivalent radius $a \sim 5$ μm, the hydrodynamic response time can be calculated to be unity, i.e. $t_H = t_e = 1$. For this analysis, the consideration of $t_H = t_e = 1$ implies that the hydrodynamic response of the capsule is over the same time scale as the evolution of the electric stresses. Also, the membrane of the capsule is considered to be purely capacitive with $\hat{C}_m = 50$ and $\hat{G}_m = 0$.
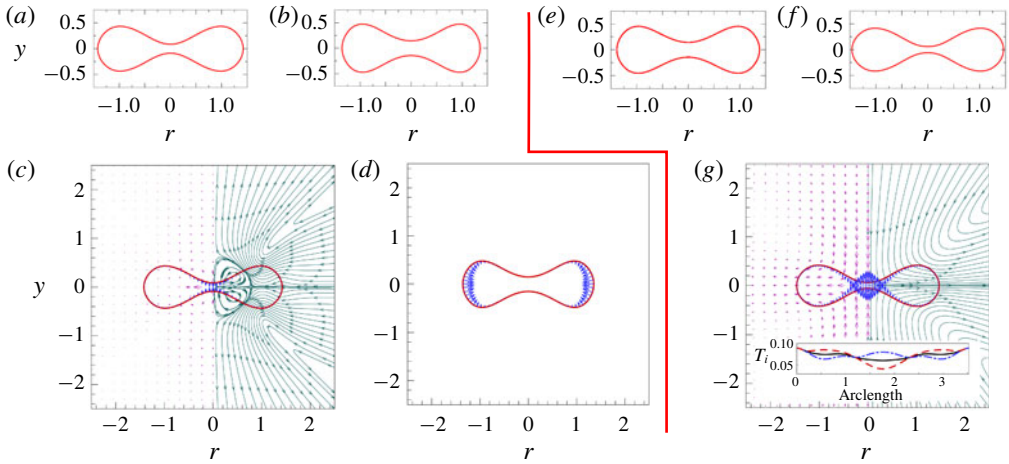
FIGURE 4. (Colour online) Observed shapes during the evolution of a biconcave-discoid capsule at (*a*) $t = 26$ and (*b*) $t = \infty$ for $Ca_e = 0.02$ and $\sigma_r = 0.1$. Corresponding streamlines (shown only in the right-hand half), velocity profile (relative magnitude of the flow is proportional to the length of the short arrows shown in left-hand half) and electric stress distribution (shown by short arrows from the interface) are shown in (*c*) and (*d*), respectively. Observed shapes during deformation at (*e*) $t = 0$ and (*f*) $t = 15$ at $Ca_e = 0.05$ and $\sigma_r = 0.1$. Streamlines, velocity profile and electric stress distribution are shown in (*g*) corresponding to the shape shown in (*e*). The variation of the meridional, T_s (——), azimuthal, T_ϕ (— · —) and mean, T_m (——) membrane tensions along the arclength are shown in the inset of (*g*).

3.2.1. *More conducting outer fluid medium: $\sigma_r = 0.1$*

When the outer fluid is more conducting than the inner fluid ($\sigma_r = 0.1$), at $Ca_e = 0.02$, a biconcave-discoid capsule initially undergoes compression at the poles (see figure 4*a,c*). In this case, the shapes are presented as 2D cross-sections in the plane parallel to the axis of symmetry, for better visualization in small deformation. At $t < t_{cap}$, the polarization vector is in the direction opposite to the applied electric field; therefore, the normal electric stresses are compressive at the poles (see figure 4*c*). Later, at $t > t_{cap}$, the membrane becomes charged, and the electric stress becomes compressive, with the maxima at the equator (see figure 4*d*). This drives the poles apart, and the capsule reaches a steady shape, as shown in figure 4(*b*). At this low capillary number, a biconcave-discoid capsule does not undergo large deformation due to the weak electric stresses at the interface.

At significantly high capillary number ($Ca_e = 0.05$), a biconcave-discoid capsule exhibits a pinched discoid with the poles coming in close contact (see figure 4*f*). At $t < t_{cap}$, strong compressive electric stresses at the poles and fluid flow from poles to the equator are observed (see figure 4*g*, corresponding to figure 4*f*). Beyond this state, the high fluid flow and electric stresses indicate possible breakup of a capsule, which manifests as a numerical singularity.

3.2.2. *More conducting inner fluid medium: $\sigma_r = 10$*

When the inner fluid medium is more conducting, the capsule does not collapse; instead, it deforms through a series of cylindrical shapes to a steady-state shape. At a small capillary number ($Ca_e = 0.3$), a biconcave-discoid capsule deforms through
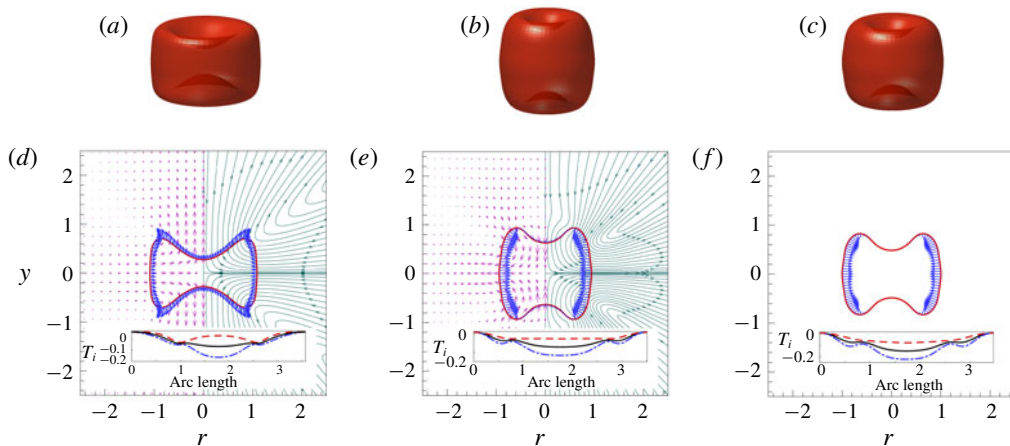
FIGURE 5. (Colour online) Observed shapes during the evolution of a biconcave-discoid capsule at (*a*) $t = 20$, (*b*) $t = 85$ and (*c*) $t = \infty$ for $Ca_e = 0.3$ and $\sigma_r = 10$. Corresponding streamlines (shown only in the right-hand half), velocity profile (relative magnitude of the flow is proportional to the length of the short arrows shown in the left-hand half) and electric stress distribution (shown by short arrows from the interface) are shown in (*d*), (*e*) and (*f*), respectively. The variation of meridional, T_s (——), azimuthal, T_ϕ (— · —) and mean, T_m (——) membrane tensions along the arclength are shown in the insets.

an intermediate cylindrical shape with concave ends (see figure 5*a*). In this case, the polarization vector aligns with the applied electric field; therefore, the electric stresses are tensile near the poles and highest at the shoulders (see figure 5*d*). Just after $t > t_{cap}$, as the membrane becomes charged, the tensile electric stresses at the poles disappear, and the compressive electric stresses develop at the equator. In this case, as the normal tensile electric stresses disappear, the intermediate shape (see figure 5*b*) relaxes back (because of the stabilizing elastic traction) to an equilibrium shape (see figure 5*c*). This equilibrium shape is the result of the balance of the elastic traction and compressive electric stress (see figure 5*f*).

At a high capillary number ($Ca_e = 0.5$), the biconcave-discoid capsule at short times deforms into cylindrical shapes with diminishing concave ends near the poles (see figure 6*a,b*) due to high tensile Maxwell stress at the poles and the shoulders (see figure 6*f,g*). In this case, since the hydrodynamic time scale is small ($t_H = t_e = 1$), the deformation progresses rapidly. At $t < t_{cap}$, due to the tensile electric stress (with the maxima near the poles, see figure 6*h*) the biconcave-discoid shape evolves into a cylindrical shape (see figure 6*c*). The tensile normal electric stress at the poles (see figure 6*i*) continues to drive the capsule to evolve into a prolate-spheroid shape (see figure 6*d*). Eventually, when the membrane becomes fully charged ($t > t_{cap}$), it attains a steady-state capped-cylindrical shape (see figure 6*e*), wherein the compressive electric stress at the equator (see figure 6*j*) is appropriately balanced by the elastic tensions.

Thus, similar to the deformation in extensional flow (see figure 2), a biconcave-discoid capsule deforms into a steady-state capped cylinder (see figure 6), but via an intermediate prolate-spheroid shape (see figure 6*d*), when the inner fluid medium is more conducting ($\sigma_r = 10$). In the former case, the deformation is driven by the hydrodynamic pressure generated by the extensional flow around the biconcave-discoid capsule, whereas in the latter case, it is due to the Maxwell electric stress developed at the interface of the capsule.
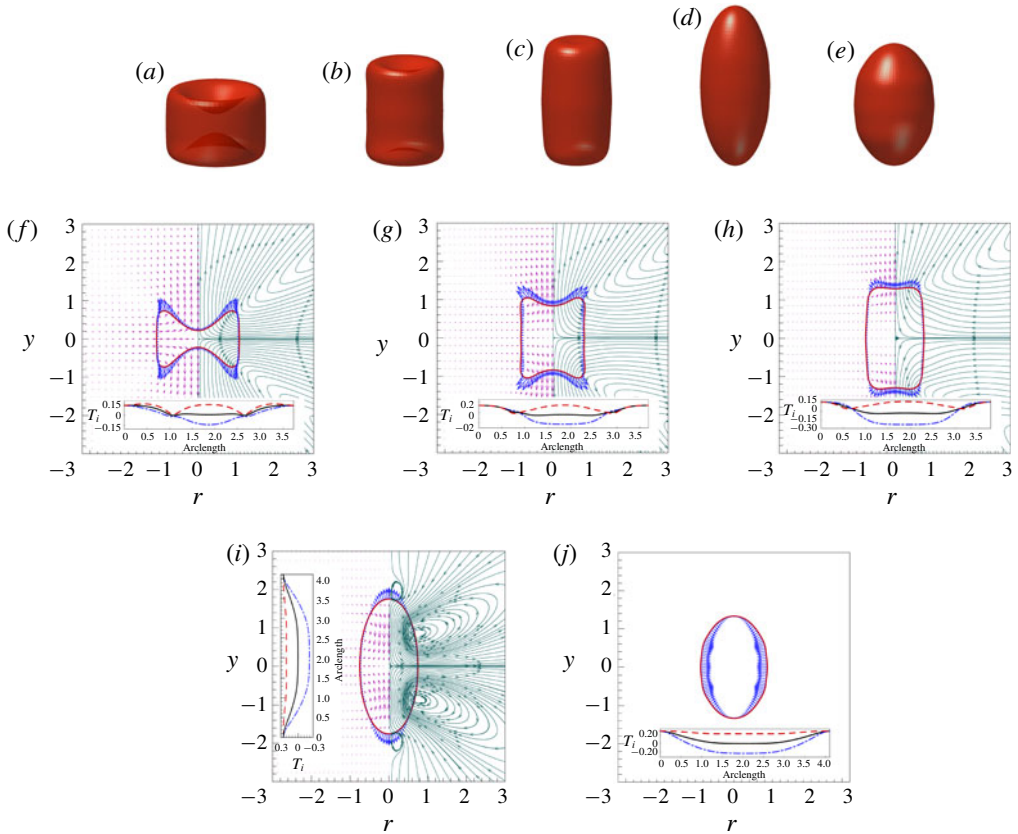
FIGURE 6. (Colour online) Observed shapes during the evolution of a biconcave-discoid capsule at (*a*) $t=10$, (*b*) $t=23$, (*c*) $t=29$, (*d*) $t=37$ and (*e*) $t=\infty$ for $Ca_e=0.5$ and $\sigma_r=10$. Corresponding streamlines (shown only in the right-hand half), velocity profile (relative magnitude of the flow is proportional to the length of the short arrows shown in the left-hand half) and electric stress distribution (shown by short arrows from the interface) are shown in (*f*), (*g*), (*h*), (*i*) and (*j*), respectively. The variation of meridional, T_s (——), azimuthal, T_ϕ (— · —) and mean, T_m (——) membrane tensions along the arclength are shown in the insets.

During the deformation, the transmembrane potential evolves due to the charging of the membrane as well as the change in the shape of the biconcave-discoid capsule. A high transmembrane potential indicates a greater tendency to electroporate. Figure 7(*a,b*) shows the variation of transmembrane potential over the interface for different intermediate shapes during the deformation at $Ca_e=0.3$ and $Ca_e=0.5$, respectively. From figure 7(*a*) it can be observed that the transmembrane potential is always higher at the shoulders until the membrane becomes fully charged, as the shape remains biconcave during the deformation (figure 5*a,b*). For the charged membrane and the steady-state shape (figure 5*c*), the transmembrane potentials from the poles to the shoulders are comparable and higher than the other locations at the interface. From figure 7(*b*) it can be observed that in the deformation at $Ca_e=0.5$ the transmembrane potential is higher at the shoulders for the cylinders with concave ends (figure 6*a–c*), whereas it is higher at the poles for the prolate-spheroid (figure 6*d–e*) shapes.
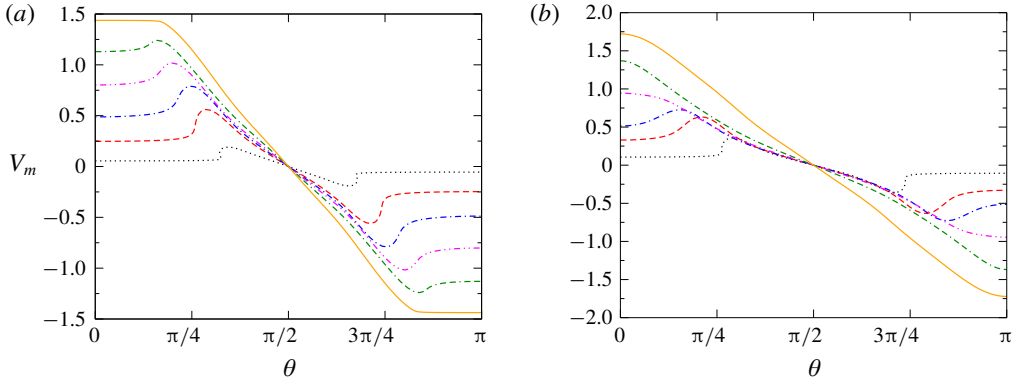
FIGURE 7. (Colour online) Transmembrane potential at the interface during the shape evolution of a biconcave-discoid capsule at $(\cdots)$ $t = 5$, (———) $t = 20$, $(\text{— } \cdot \text{ —})$ $t = 35$, $(-\cdot\cdot)$ $t = 55$, $(---)$ $t = 85$ and (———) $t = \infty$ for $Ca_e = 0.3$ (a), and at $(\cdots)$ $t = 10$, (———) $t = 23$, $(\text{— } \cdot \text{ —})$ $t = 29$, $(-\cdot\cdot)$ $t = 37$, $(--)$ $t = 50$ and (———) $t = \infty$ for $Ca_e = 0.5$ (b).
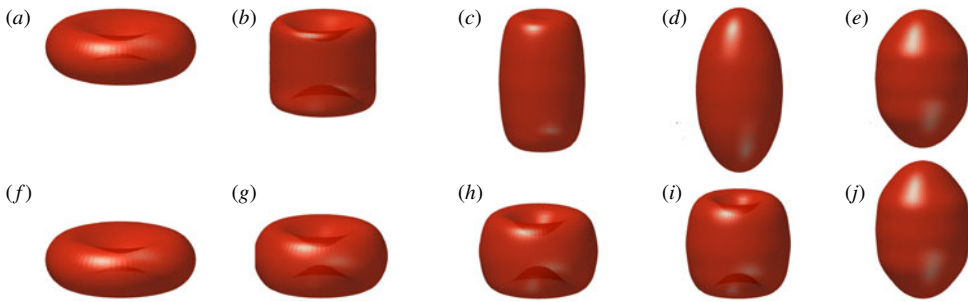
FIGURE 8. (Colour online) Observed shapes during the deformation of a biconcave-discoid capsule for $Ca_e = 0.4$ and $\sigma_r = 10$ at (a) $t = 0$, (b) 20, (c) 42, (d) 52 and (e) ∞, considering $k_f = 1$ and at (f) $t = 0$, (g) 500, (h) 1500, (i) 5000 and (j) ∞, considering $k_f = 0.01$.

When the hydrodynamic response time and the electric response time are same, $t_H = t_e = 1$, i.e. $k_f = 1$, at the critical capillary number ($Ca_e = 0.4$), a biconcave discoid evolves into a capped cylinder through the intermediate shapes, such as biconcave cylinder and stretched prolate spheroid, similar to the case of $Ca_e = 0.5$ (see figure 6). At this capillary number ($Ca_e = 0.4$), the shape evolution is shown in figure 8(a–e). To demonstrate the effect of slow hydrodynamics, the shape evolutions of a biconcave-discoid capsule at $Ca_e = 0.4$ and $\sigma_r = 10$ are presented in figure 8(f–j) considering $k_f = 0.01$. In this case, a biconcave-discoid capsule does not respond instantly to the developed electric stresses at the interface. Therefore, for $t < t_{cap}$, the intermediate stretched biconcave-cylindrical (see figure 8b), stretched cylindrical (see figure 8c), and highly deformed prolate-spheroid (see figure 8d) shapes are missing in the deformation considering $k_f = 0.01$. Instead, the biconcave-discoid capsule undergoes a slow deformation through few intermediate shapes (see figure 8g–i), and eventually attains a capped-cylindrical shape (see figure 8j) at the equilibrium. Hence, for different hydrodynamic response times (here, $t_H = 1$ and 100, i.e. $k_f = 1$ and 0.01), even though the final equilibrium shape, a biconcave-discoid capsule attains, is same (see figure 8e and figure 8j), the pathways for the shape evolution are different.

3.3. *Dynamics of an RBC in AC electric fields*

The electrohydrodynamic deformation of a biconcave-discoid capsule can be extended to explore its suitability for studying an RBC in an electric field. In physiological conditions, the non-dimensional parameters relevant for an RBC are: viscosity ratio $\lambda = 5$, ratio of dielectric constants $\epsilon_r = 0.6$, conductivity ratio $\sigma_r = 1.054$, non-dimensional capacitance $\hat{C}_m = 282$ and non-dimensional conductance $\hat{G}_m = 6.75 \times 10^{-7}$. Considering scaling parameters as used in the case of deformation of a biconcave-discoid capsule, for the deformation of an RBC, the non-dimensional hydrodynamic time scale is very large (non-dimensional $t_H = 0.625 \times 10^6$). Therefore, the kinematic factor $k_f = 1/t_H \sim O(10^{-6})$ implies that a negligible displacement (2.14) of the interface will take place in a specific numerical time step, $\Delta t \sim O(\tilde{t}_e)$, suggesting that the computation time required for reaching a steady shape could be prohibitively high.

Since the hydrodynamic response time is very high compared to the electric time scale, the electric field at the interface reaches an equilibrium value (with respect to the transmembrane potential that corresponds to the charging time of the membrane and the frequency of the applied field) even before the capsule starts responding to the electric stress developed at the interface. The electric field (2.7) is, therefore, solved with the capacitor time scale, $\tilde{t}_{cap} = \hat{C}_m \times$ electric time scale (i.e. $\tilde{t}_{cap} = \hat{C}_m \times \tilde{t}_e = 282 \times \epsilon_e \epsilon_0 / \sigma_e$), and the transmembrane potential is allowed to reach a steady value at a particular shape of the RBC. Moreover, as the charge relaxation in both the inner and outer fluids are very fast ($\epsilon_e / \sigma_e \ll 1$ and $\epsilon_i / \sigma_i \ll 1$), a simplification of the electric current continuity (2.8) across the interface is made as

$$\sigma_r E_{n,i} = E_{n,e} = \frac{\mathrm{d}V_m}{\mathrm{d}t_e}. \tag{3.2}$$

Subsequently, the hydrodynamic equation for RBC deformation (2.12) is solved with the already calculated equilibrium electric stress, considering the hydrodynamic response time ($t_H = \mu_e a / E_s$) as the scaling parameter for the time.

All the variables but time (here $t_e = \tilde{t}/\hat{C}_m \times \tilde{t}_e$) for solving the electric potential (2.7) are scaled with the scaling parameters used for the solution of electrostatics in the case of a biconcave-discoid elastic capsule in a DC electric field, as discussed in the previous section. Thus, $1/(\hat{C}_m \times \tilde{t}_e)$ is used for scaling the frequency of the applied field. For solving the hydrodynamic boundary integral equation (2.12), the hydrodynamic time scale is used for scaling.

The hydrodynamic force is balanced by the non-hydrodynamic forces similar to the case of deformation of an elastic capsule in a DC electric field (3.1). In this case, time-averaged electric stress (ignoring the time-periodic stress that has instantaneous dynamics but zero average) is used in the calculation of interfacial velocity (in (2.12)). For faster numerical calculations, the viscosity ratio is considered to be unity, $\lambda = 1$. The kinematic condition (2.14) for the shape evolution from the calculated interfacial velocity, because of $k_f = 1$, simplifies to

$$\boldsymbol{x}(t + \Delta t) = \boldsymbol{x}(t) + \boldsymbol{u}(\boldsymbol{x})\Delta t. \tag{3.3}$$

The analysis of the deformation of an RBC in AC electric fields is conducted at a high frequency of the applied field ($\omega = 2.5$, corresponding to $\sim$10 MHz). This
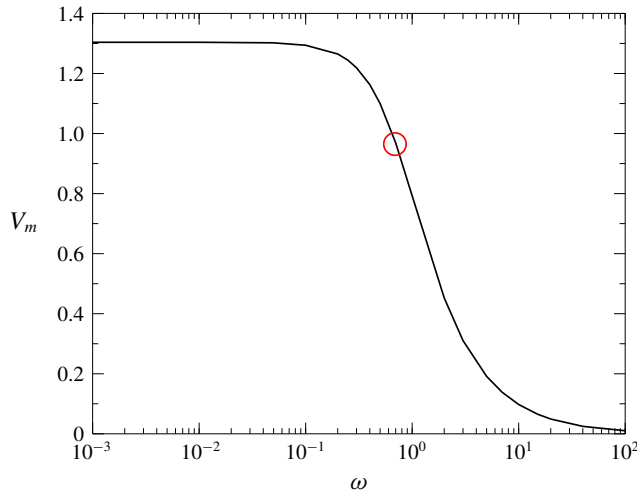
FIGURE 9. (Colour online) Transmembrane potential of the static shape of an RBC as a function of frequency. Marker point ○ represents t_{cap}^{-1}.

is important in suggested experiments, wherein the transmembrane potential (V_m) has to be restricted to a very low value to prevent the possibility of electroporation (see figure 9) (Joshi & Hu 2012; Das & Thaokar 2018a). The electric capillary number (Ca_e) remains the same as used in the case of the deformation of a biconcave-discoid capsule in a DC field. In the case of the RBC deformation, $Ca_e = 1$ is equivalent to the applied electric field strength of 0.45 kV cm^{-1}, much below the typical 1 kV cm^{-1} or higher used in electroporation studies.

At $Ca_e = 0.5$, the small electric stresses at the interface lead to a small deformation of the RBC (see figure 10a,b). The transmembrane potential reaches an equilibrium value before the hydrodynamic calculation begins. Since $\omega < t_{cap}^{-1}$, the electric stress is purely compressive, with the maxima at the equator (similar to the case of a biconcave-discoid capsule in DC electric field, shown in figure 5f). This compressive electric stress is responsible for the deformation of the RBC into a cylinder with concave ends. At larger capillary number ($Ca_e = 1$), a substantial increase in the deformation is observed (see figure 10g,h). From figure 10(c,d,i,j), it can be observed that the azimuthal, meridional and mean elastic tensions are compressive near the equator and tensile near the poles.

Consideration of the area dilatation parameter $C = 1$ allows a significant change in the area during the deformation of an RBC, i.e. 4.7 % and 13.8 % at $Ca_e = 0.5$ and $Ca_e = 1$, respectively. At a higher value of the area dilatation parameter ($C = 10$), the constraint on the change in area (0.82 % and 1.75 % at $Ca_e = 0.5$ and 1, respectively) restricts the deformation of an RBC. Considering $C = 10$, the shapes observed during the deformation of an RBC at $Ca_e = 0.5$ and 1 are shown in figure 10(e,f,k,l), respectively. It can be easily visualized that the deformation of an RBC considering $C = 10$ is considerably less compared to the deformation with $C = 1$.

To understand the mechanical integrity of the cell membrane to the applied electric field, the analysis of the transmembrane potential, during the deformation is important. Figure 11(a) shows that at $Ca_e = 0.5$, the transmembrane potential of the membrane at the north pole of an RBC during the calculation of the average electric stress in a cycle of the applied electric field varies with time. Figure 11(b) represents the
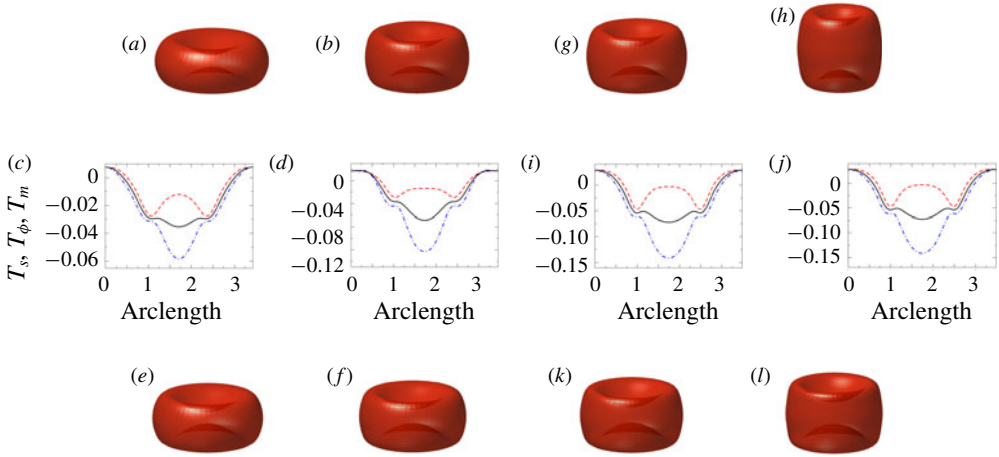
FIGURE 10. (Colour online) Shapes observed during the deformation of an RBC at (*a*) $t = 10$ and (*b*) $t = \infty$ for $Ca_e = 0.5$ and 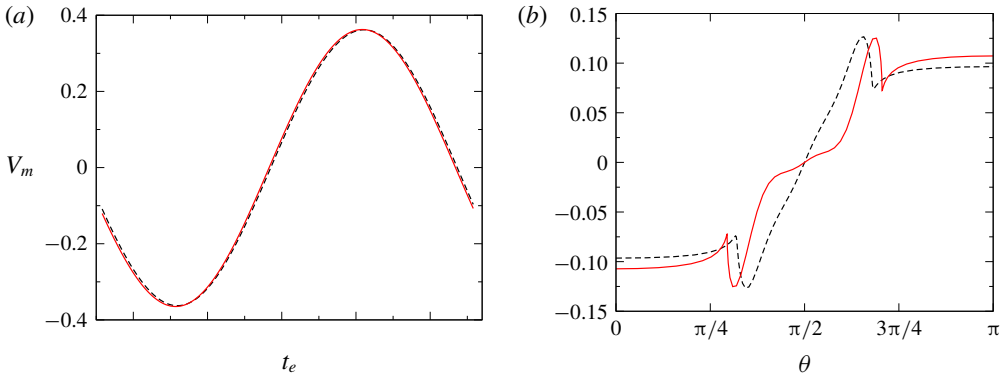at (*g*) $t = 20$ and (*h*) $t = \infty$ for $Ca_e = 1$ in an AC field with $\omega = 2.5$, considering $C = 1$. Variation of the meridional, T_s (——), azimuthal, T_ϕ (— · —) and mean, T_m (——) elastic tensions along the arclength for the corresponding cases are shown in (*c*,*d*) and (*i*,*j*), respectively. Shapes observed during the deformation of an RBC at (*e*) $t = 24$ and (*f*) $t = \infty$ for $Ca_e = 0.5$ and at (*k*) $t = 20$ and (*l*) $t = \infty$ for $Ca_e = 1$, considering $C = 10$.

FIGURE 11. (Colour online) At $Ca_e = 0.5$. (*a*) Transmembrane potential at the north pole in a single cycle of the applied electric field during the calculation of average electric stress at (– –) $t = 10$ and (——) $t = \infty$. (*b*) Variation of the transmembrane potential at the end of the particular cycle of the applied field over the arclength at (– –) $t = 10$ and (——) $t = \infty$, corresponding to figure 10(*a*,*b*), respectively.

variation of the transmembrane potential of the interface at the end of the cycle. It can be clearly observed in figure 11(*b*) that the shoulders attain the maximum transmembrane potential, suggesting the possibility of electroporation in those regions. Similar behaviour of the membrane is suggested in figure 12(*a*,*b*) for the deformation of an RBC at $Ca_e = 1$.

In an experimental condition with a low-conducting outer fluid medium (in this case, $\sigma_r = 10$), an RBC undergoes large deformation even at a low capillary number
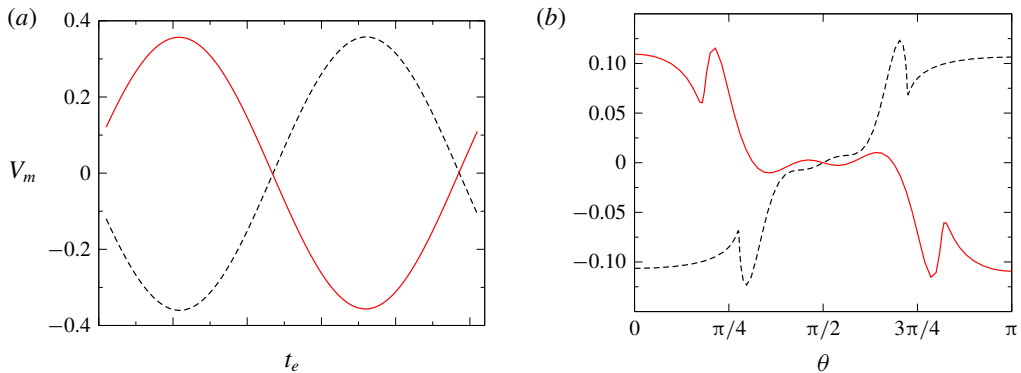
FIGURE 12. (Colour online) At $Ca_e = 1$. (a) Transmembrane potential at the north pole in a single cycle of the applied electric field during the calculation of average electric stress at (--) $t = 20$ and (——) $t = \infty$. (b) Variation of the transmembrane potential at the end of the particular cycle of the applied field over the arclength at (--) $t = 20$ and (——) $t = \infty$, corresponding to figure 10(g,h), respectively.
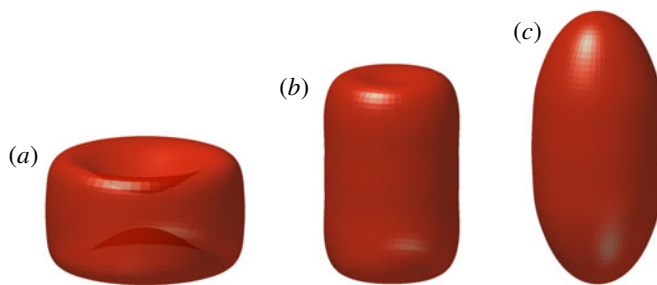

FIGURE 13. (Colour online) Shapes observed during the deformation of an RBC at (a) $t = 10$, (b) $t = 70$ and (c) $t = \infty$ for $Ca_e = 0.5$ in an AC field with $\omega = 2.5$, considering $C = 1$ and $\sigma_r = 10$.

($Ca_e = 0.5$). The strong compressive electric stress causes an RBC to deform through a cylindrical shape with biconcave ends (see figure 13a) to a cylinder (see figure 13b), finally resulting in a prolate spheroid (see figure 13c). Unlike the case of a biconcave-discoid capsule, an RBC does not show the intermediate large deformation (as observed in figure 6d), as the partial charging of the membrane results in consistent tensile electric stress at the poles and compressive electric stress at the equator. In this case, since a small value of area dilatation parameter ($C = 1$) is used, a significant change in the area is observed. From figure 14(a,b), it can be observed that for the intermediate cylinder with concave ends (figure 13a) and a cylindrical shape (figure 13b) the transmembrane potential is the highest at the shoulders. On the other hand, when the RBC evolves into a prolate spheroid at the time-averaged steady state, the transmembrane potential is maximum at the poles, thereby suggesting the possibility of electroporation at the poles.

4. Conclusions

Red blood cells and biconcave-discoid capsules can encounter extensional flow fields at the junctions and size-varying capillaries in blood vessels. Moreover, the
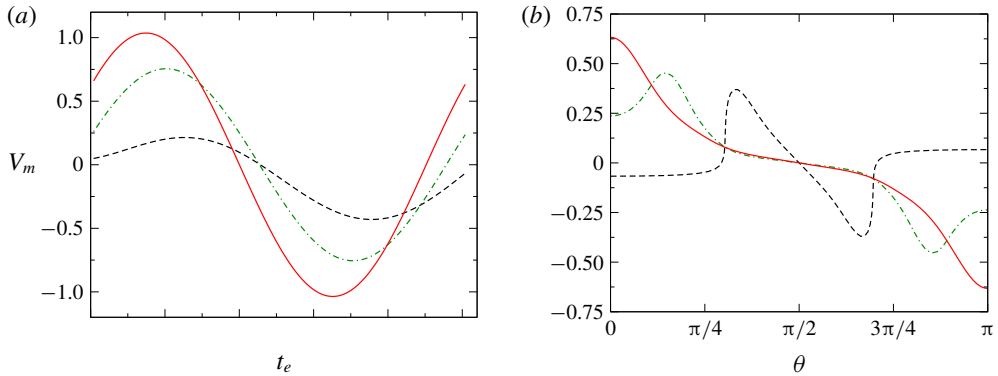
FIGURE 14. (Colour online) At $Ca_e = 0.5$ and $\sigma_r = 10$. (*a*) Transmembrane potential at the north pole in a single cycle of the applied electric field during the calculation of the average electric stress at (‑‑) $t = 10$, (— · —) $t = 70$ and (——) $t = \infty$. (*b*) Variation of the transmembrane potential at the end of the particular cycle of the applied field over the arclength at (‑‑) $t = 10$, (— · —) $t = 70$ and (——) $t = \infty$, corresponding to figure 13(*a–c*), respectively.

biconcave-discoid capsules are subjected to electric fields in applications such as electroporation and dielectrophoresis. This study, therefore, investigates the responses of biconcave discoids in extensional flow and electric fields. In the analysis of the dynamics of deformations, a transition from a biconcave-discoid shape to prolate-spheroid and capped-cylindrical shapes is predicted. The shape changes of a biconcave discoid in the above-mentioned cases are relevant because they determine the extent of momentum and mass transfer between the capsule and the surrounding fluid. Additionally, these shape changes can also be used to characterize the electromechanical properties of biconcave discoids. The dynamics of a biconcave discoid is sensitively dependent upon elastic properties such as Youngs modulus, the membrane dilatation parameter, electric properties such as the membrane capacitance as well as the fluid conductivities, and the ratio of the electric time scale and the hydrodynamic time scale.

In an extensional flow, a biconcave-discoid capsule undergoes axisymmetric deformation while developing membrane tension. Recalling the dimensional variables for RBCs from table 1, the estimated tension in the transition to prolate spheroid is $\sim O(1)$ mN m^{-1} and the corresponding strain rate is $\sim O(10)$ s^{-1}. Therefore, considering the suggested tolerance limit of membrane tension in the literature (Evans *et al.* 1976), there is a possibility of an RBC undergoing the biconcave-discoid to prolate-spheroid transition without the rupture of the cell. In the case of an elastic capsule, with comparatively larger membrane elastic modulus, a high strain rate is required for the biconcave-discoid to prolate-spheroid transition, resulting in the development of higher membrane tension. The experimental study concerning the in-plane orientation of an RBC in four-roll elongational flow (Levant & Steinberg 2016), along with our computational analysis, suggests a possibility of visualization of the biconcave-discoid to prolate-spheroid transition in experiments.

The electrohydrodynamic steady-state deformation of a spherical capsule is independent of the conductivity ratio (Das & Thaokar 2018*b*), whereas for a biconcave-discoid capsule the steady-state deformation is strongly dependent on the conductivity ratio. The analysis shows that when $\sigma_r = 0.1$, high Ca_e can lead

to breakup, whereas for $\sigma_r = 10$, the capsule attains a steady-state deformed shape. Further, from the analysis, it is found that the kinematic factor (k_f, consequently, t_H) influences the dynamics of the capsule deformation. For different k_f, even though the steady-state electrohydrodynamic deformation is the same, the pathways to reach the steady state are different. Moreover, the analysis of the deformation of an RBC in an electric field shows a weak response due to the typical values of the parameters in physiological conditions. In experimental conditions, a lower electrical conductivity of the outer fluid media makes the RBC sensitive to the applied AC electric field.

There are significant differences between the transition seen in extensional flow, capsules in DC electric fields, and RBCs in AC fields. A biconcave-discoid capsule and an RBC undergo axisymmetric deformation in extensional flow due to the pressure profile which develops because of the complex geometry. In an extensional flow, capped-cylindrical and prolate-spheroid shapes are seen at low and high capillary numbers, respectively. On the other hand, the deformation in an applied uniform electric field is due to the Maxwell electric stress at the interface. In extensional flow, the maximum elastic tension develops at the shoulders of the biconcave-discoid shapes, and the tension is maximum at the poles when the biconcave discoid evolves into a prolate spheroid or capped cylinder. Therefore, the possible rupture of the membrane could be at the shoulders or the poles in extensional flow. In an electric field, a similar biconcave-discoid to capped-cylindrical shape transition is possible, although through different pathways that depend upon the fields (DC and AC) and k_f. In the biconcave-discoid and biconcave-cylindrical shapes, the maximum elastic tension and transmembrane potential develop at the poles and shoulders of the deformed shape, respectively.

Thus for an RBC in an electric field, since the elastic tension is much smaller than the threshold value, for mechanical rupture, a membrane can instead electroporate at the shoulders or the poles corresponding to the maximum value of transmembrane potential. The deformation can be conducted under extensional flow of strain rate $\sim O(10)$ s^{-1} and under DC and AC (frequency $\sim O(1)$ MHz) fields of strength $\sim O(1)$ kV cm^{-1} for the rheological analysis and estimation of mechanical properties of a biconcave-discoid capsules. However, both the methods have merits and demerits. While the electrodeformation experiments are easy to conduct, the strength of the typical electric field predicted in our analysis could cause electroporation in some systems. On the other hand, although poration and lysis are discounted in extensional flow, the experiments are difficult to conduct as they require sophisticated set-ups (De Loubens *et al.* 2015; Levant & Steinberg 2016). The measure of maximum elastic tensions in capsules and RBCs in the flow and electric field will help in understanding the mechanical stability of the capsule, and thereby help improvements in designing a capsule for specific applications.

Appendix A. Additional information

Validation: deformation of oblate spheroids in extensional flow.

The developed numerical code to study the deformation of a biconcave-discoid capsule and RBC is validated with the results reported by Pozrikidis (1990) for the analysis of its deformation in a uniaxial extensional flow. In both our analysis and
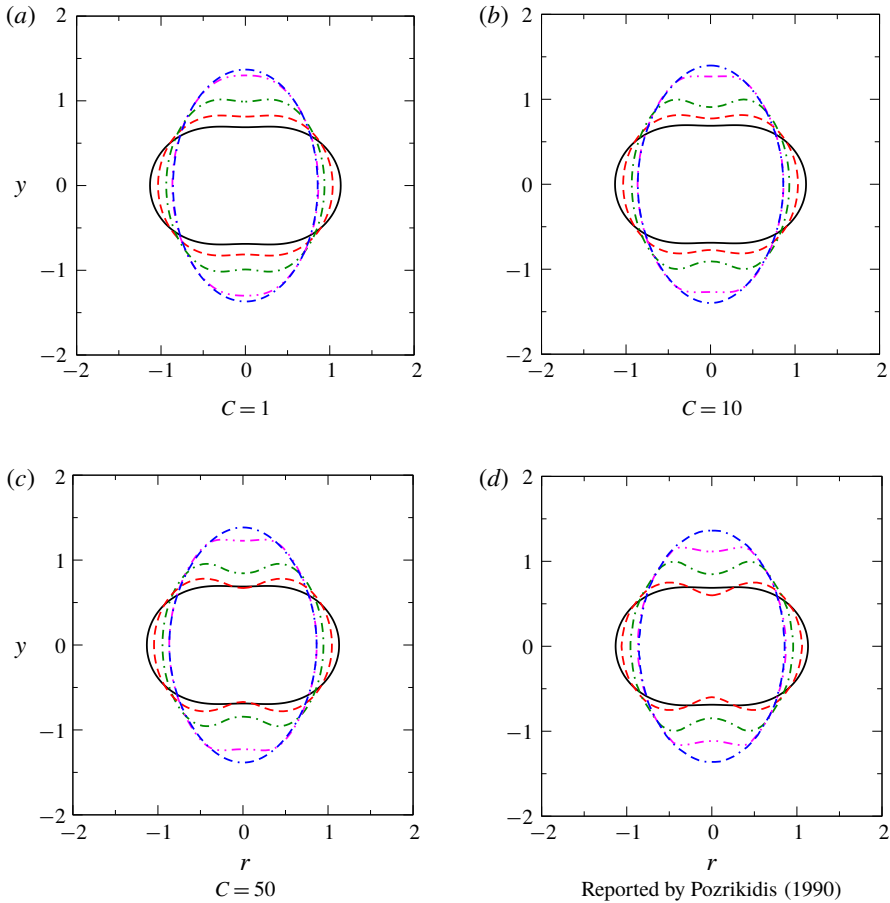
FIGURE 15. (Colour online) Comparison of boundary integral simulations at $k_s = 30$ and the reported (Pozrikidis 1990) evolution at $k = 10$ of an oblate-spheroid shape perturbed with a second-degree Legendre mode ($\epsilon = -0.3$). In each panel (——) $t = 0$, (— —) $t = 0.095$, (— · —) $t = 0.235$, (–··) $t = 0.540$ and (——·) $t = \infty$. Boundary integral simulation results (*a–c*) and reported (Pozrikidis 1990) shape evolution (*d*).

that of Pozrikidis (1990), the axisymmetric boundary integral method is used. The stress-free shapes of oblate spheroids are considered as the initial shape of the capsule, which is perturbed from the sphere with a second-degree Legendre polynomial, and the equivalent volume is maintained as unity, as assumed by Pozrikidis (1990). To define oblate-spheroid shapes, the coefficients of the Legendre polynomial are considered; these are $\epsilon = -0.3$ and $\epsilon = -0.5$ for two different cases. Similar scalings of variables as reported by Pozrikidis (1990) are used in this validation of the numerical boundary integral code.

The neo-Hookean membrane constitutive equation is a special case of the Mooney–Rivlin constitutive equations and is applicable for isotropic membranes. Pozrikidis (1990) considered a neo-Hookean membrane constitutive law to describe a RBC, where the tension components (see figure 1*d*) in the meridional and azimuthal
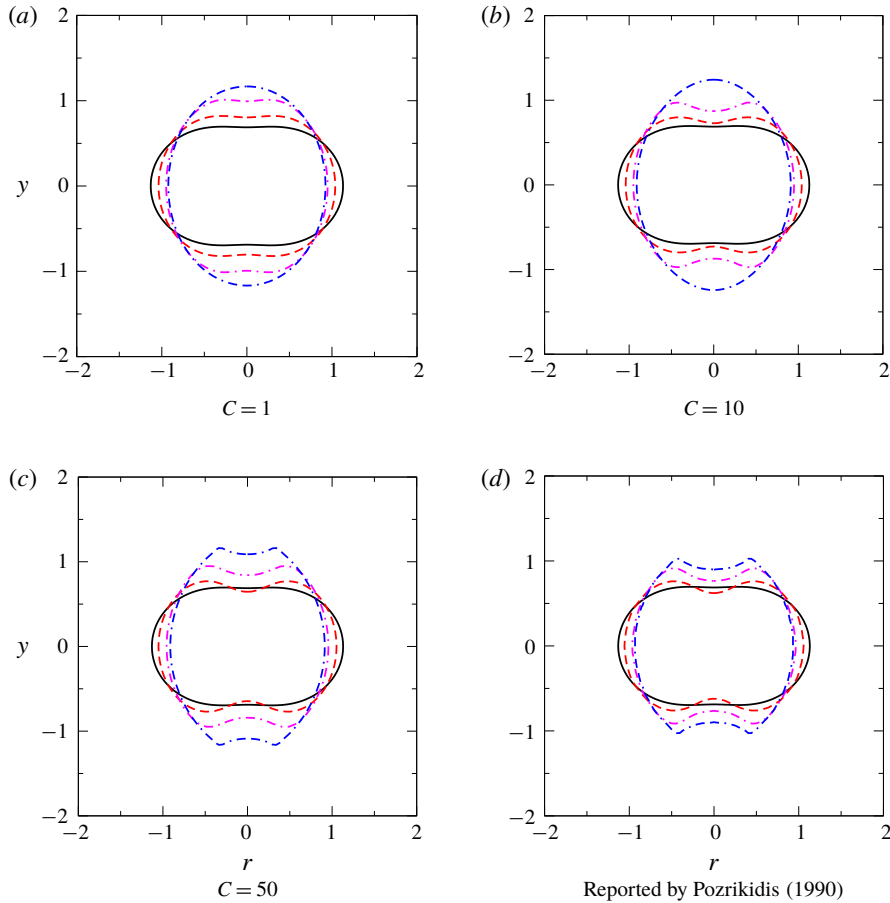
FIGURE 16. (Colour online) Comparison of boundary integral simulations at $k_s = 60$ and the reported (Pozrikidis 1990) evolution at $k = 20$ of an oblate-spheroid shape perturbed with a second-degree Legendre mode ($\epsilon = -0.3$). In each panel (——) $t = 0$, (— —) $t = 0.1$, (— · —) $t = 0.3$ and (— — ·) $t = \infty$. Boundary integral simulation results (*a*–*c*) and reported (Pozrikidis 1990) shape evolution (*d*).

directions are given by

$$\tilde{T}_{s,\phi}^{MR} = \frac{G_{MR}}{\lambda_s \lambda_\phi} \left(\lambda_s^2 - \frac{1}{(\lambda_s \lambda_\phi)^2} \right), \tag{A 1}$$

where G_{MR} is the shear modulus in the Mooney–Rivlin model. To assert a negligible change in area, Pozrikidis (1990) imposed the incompressibility condition

$$\tilde{u} \cdot j + \tilde{\sigma} t \cdot \frac{\partial \tilde{u}}{\partial s} = 0, \tag{A 2}$$

where the notations used by Pozrikidis (1990) are that $\tilde{\sigma}$ is the radial distance in the cylindrical coordinate system, $\tilde{u}$ is the interfacial velocity, j is the local surface unit normal, t is the local tangent vector, and s is the arclength.
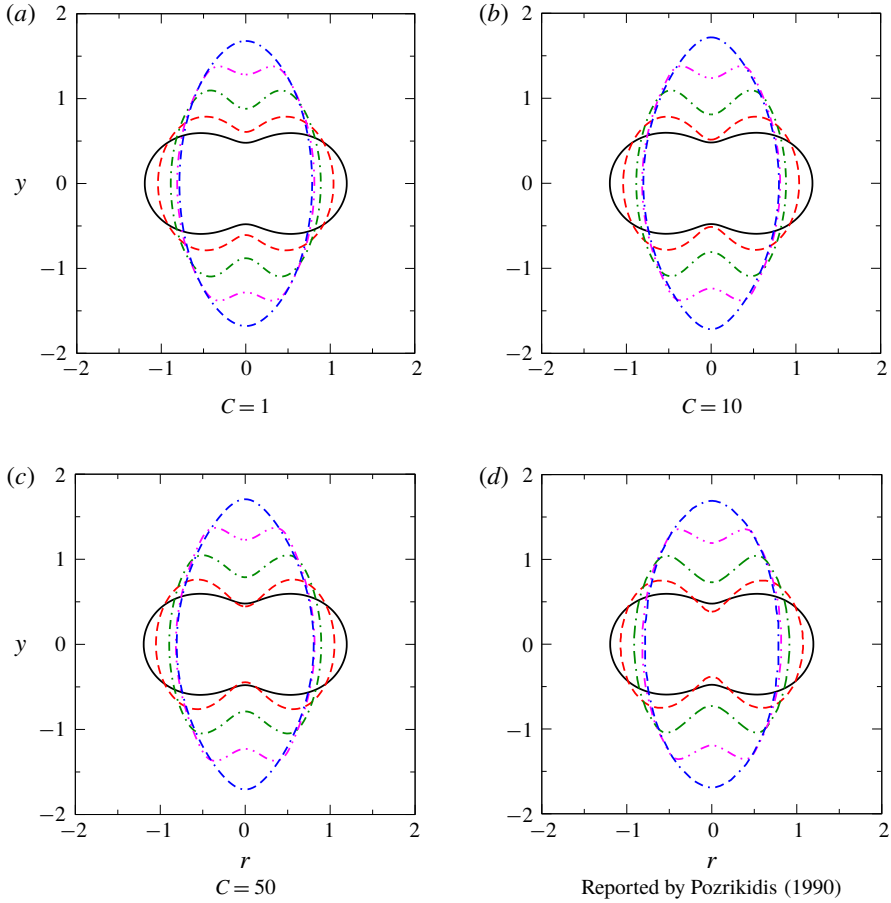
FIGURE 17. (Colour online) Comparison of boundary integral simulations at $k_s = 15$ and the reported (Pozrikidis 1990) evolution at $k = 5$ of an oblate-spheroid shape perturbed with second-degree Legendre mode ($\epsilon = -0.5$). In each panel (——) $t = 0$, (— —) $t = 0.15$, (— · —) $t = 0.375$, (–··) $t = 0.682$ and (——·) $t = \infty$. Boundary integral simulation results (*a*–*c*) and reported (Pozrikidis 1990) shape evolution (*d*).

In the reported analysis (Pozrikidis 1990), the elastic modulus is replaced with the non-dimensional variable $k = G_{MR}/\mu ea$. In our numerical computations, we have used the relation between the Skalak modulus (G_{SK}) and the surface Young modulus (E_s), given by

$$E_s = 2G_{SK}\frac{1 + 2C}{1 + C}, \tag{A 3}$$

where C is the membrane dilatation parameter (Barthès-Biesel *et al.* 2002). For the Skalak model, the non-dimensional elastic modulus is $k_s = E_s/\mu ea$. Therefore, the non-dimensional elastic modulus considered in this analysis is three times that of the non-dimensional elasticity considered by Pozrikidis (1990), i.e. $k_s = 3 \times k$. Moreover, the area conservation is not explicitly implemented in the present work, since the parameter C can be independently used to enforce area conservation.

In figures 15, 16, and 17, the comparisons of shape evolution with time are shown for the oblate-spheroid shapes with perturbation coefficients of a second-degree

C	Change in area (%)
1	2.8
10	2.15
50	1.05

TABLE 2. Percentage change in area at different membrane parameter C for $\epsilon = -0.3$ and $k_s = 30$.

C	Change in area (%)
1	2.81
10	1.78
50	0.62

TABLE 3. Percentage change in area at different membrane parameter C for $\epsilon = -0.3$ and $k_s = 60$.

C	Change in area (%)
1	4.7
10	2.9
50	1.22

TABLE 4. Percentage change in area at different membrane parameter C for $\epsilon = -0.5$ and $k_s = 15$.

Legendre polynomial $\epsilon = -0.3$, -0.3 and -0.5, respectively, in extensional flow. The reported (Pozrikidis 1990) shape evolutions of oblate spheroids with $\epsilon = -0.3$ at $k = 10$ and $k = 20$ are similar to the obtained boundary integral simulation considering $k_s = 30$ and $k_s = 60$, respectively. Also, similar dynamics are observed for the deformation of an oblate spheroid with $\epsilon = -0.5$ reported for $k = 5$ and calculated with $k_s = 15$. The percentage changes in the surface area during the deformation of the capsule are shown in tables 2, 3 and 4 for the boundary integral simulation with $k_s = 30$, $k_s = 60$ and $k_s = 15$, respectively. From the tables 2–4 and figures 15–17, it can be observed that with an increase in the area dilatation parameter, C, the change in area decreases and the simulated result with high area dilatation parameter produces similar results to those reported by Pozrikidis (1990).

REFERENCES

ASHE, J. W., BOGEN, D. K. & TAKASHIMA, S. 1988 Deformation of biological cells by electric fields: theoretical prediction of the deformed shape. *Ferroelectrics* **86**, 311–324.

BARTHÈS-BIESEL, D., DIAZ, A. & DHENIN, E. 2002 Effect of constitutive laws for two-dimensional membranes on flow-induced capsule deformation. *J. Fluid Mech.* **460**, 211–222.

BEVING, H., ERIKSSON, L. E. G., DAVEY, C. L. & KELL, D. B. 1994 Dielectric properties of human blood and erythrocytes at radio frequencies (0.2–10 MHz); dependence on cell volume fraction and medium composition. *Eur. Biophys. J.* **23** (3), 207–215.

CHAMPION, J. A., KATARE, Y. K. & MITRAGOTRI, S. 2007 Particle shape: a new design parameter for micro- and nanoscale drug delivery carriers. *J. Control. Release* **121** (1–2), 3–9.

CHANG, S., TAKASHIMA, S. & ASAKURA, T. 1985 Volume and shape changes of human erythrocytes induced by electrical fields. *J. Bioelectr.* **4** (2), 301–316.

CORDASCO, D. & BAGCHI, P. 2017 On the shape memory of red blood cells. *Phys. Fluids* **29** (4), 041901.

CRUZ, J. M. & GARCÍA-DIEGO, F. J. 1998 Dielectrophoretic motion of oblate spheroidal particles. measurements of motion of red blood cells using the Stokes method. *J. Phys.* D **31** (14), 1745–1751.

DAS, S. & THAOKAR, R. M. 2018a Large deformation electrohydrodynamics of a Skalak elastic capsule in ac electric field. *Soft Matt.* **14**, 1719–1736.

DAS, S. & THAOKAR, R. M. 2018b Large-deformation electrohydrodynamics of an elastic capsule in a DC electric field. *J. Fluid Mech.* **841**, 489–520.

DE LOUBENS, C., DESCHAMPS, J., BOEDEC, G. & LEONETTI, M. 2015 Stretching of capsules in an elongation flow, a route to constitutive law. *J. Fluid Mech.* **767**, R3.

DECUZZI, P., PASQUALINI, R., ARAP, W. & FERRARI, M. 2008 Intravascular delivery of particulate systems: Does geometry really matter? *Pharmaceut. Res.* **26** (1), 235–243.

DIAZ, A., PELEKASIS, N. & BARTHÈS-BIESEL, D. 2000 Transient response of a capsule subjected to varying flow conditions: Effect of internal fluid viscosity and membrane elasticity. *Phys. Fluids* **12** (5), 948–957.

DU, E., DAO, M. & SURESH, S. 2014 Quantitative biomechanics of healthy and diseased human red blood cells using dielectrophoresis in a microfluidic system. *Extreme Mech. Lett.* **1**, 35–41.

ENGELHARDT, H. & SACKMANN, E. 1988 On the measurement of shear elastic moduli and viscosities of erythrocyte plasma membranes by transient deformation in high frequency electric fields. *Biophys. J.* **54** (3), 495–508.

EVANS, E. & FUNG, Y.-C. 1972 Improved measurements of the erythrocyte geometry. *Microvasc. Res.* **4** (4), 335–347.

EVANS, E. A. 1980 Minimum energy analysis of membrane deformation applied to pipet aspiration and surface adhesion of red blood cells. *Biophys. J.* **30**, 265–284.

EVANS, E. A., WAUGH, R. & MELNIK, L. 1976 Elastic area compressibility modulus of red cell membrane. *Biophys. J.* **16** (2), 585–595.

FISCHER, T. M. 2004 Shape memory of human red blood cells. *Biophys. J.* **86** (5), 3304–3313.

FREUND, J. B. 2014 Numerical simulation of flowing blood cells. *Annu. Rev. Fluid Mech.* **46** (1), 67–95.

FRIEND, A., FINCH, E. & SCHWAN, H. 1975 Low frequency electric field induced changes in the shape and motility of amoebas. *Science* **187**, 357–359.

GASS, G. V., CHERNOMORDIK, L. V. & MARGOLIS, L. B. 1991 Local deformation of human red blood cells in high frequency electric field. *Biochim. Biophys. Acta* **1093** (2), 162–167.

GROSSE, C. & SCHWAN, H. P. 1992 Cellular membrane potentials induced by alternating fields. *Biophys. J.* **63** (6), 1632–1642.

GUCKENBERGER, A. & GEKLE, S. 2017 Theory and algorithms to compute Helfrich bending forces: A review. *J. Phys.: Condens. Matter* **29** (20), 203001.

HAIDEKKER, M. A., TSAI, A. G., BRADY, T., STEVENS, H. Y., FRANGOS, J. A., THEODORAKIS, E. & INTAGLIETTA, M. 2002 A novel approach to blood plasma viscosity measurement using fluorescent molecular rotors. *Am. J. Physiol.* **282** (5), H1609–H1614.

HELFRICH, W. & DEULING, H. J. 1975 Macroscopic features. d) Biological systems: some theoretical shapes of red blood cells. *J. de Phys. Colloques* **36** (C1), 327–329.

HENON, Y., SHEARD, G. J. & FOURAS, A. 2014 Erythrocyte deformation in a microfluidic cross-slot channel. *RSC Adv.* **4**, 36079–36088.

HU, W. F., KIM, Y. & LAI, M.-C. 2014 An immersed boundary method for simulating the dynamics of three-dimensional axisymmetric vesicles in Navier–Stokes flows. *J. Comput. Phys.* **257** (Part A), 670–686.

JOSHI, R. P. & HU, Q. 2012 Role of electropores on membrane blebbinga model energy-based analysis. *J. Appl. Phys.* **112** (6), 064703.

JOSHI, R. P., HU, Q., SCHOENBACH, K. H. & BEEBE, S. J. 2002 Simulations of electroporation dynamics and shape deformations in biological cells subjected to high voltage pulses. *IEEE Trans. Plasma Sci.* **30** (4), 1536–1546.

KARYAPPA, R. B., DESHMUKH, S. D. & THAOKAR, R. M. 2014 Deformation of an elastic capsule in a uniform electric field. *Phys. Fluids* **26** (12), 122108.

KONONENKO, V. L. & SHIMKUS, J. K. 2000 Stationary deformations of erythrocytes by high-frequency electric field. *Bioelectrochemistry* **52** (2), 187–196.

KONONENKO, V. L. & SHIMKUS, J. K. 2002 Transient dielectro-deformations of erythrocyte governed by time variation of cell ionic state. *Bioelectrochemistry* **55** (1), 97–100.

KONONENKO, V. L. 2002 Dielectro-deformations and flicker of erythrocytes: fundamental aspects of medical diagnostics applications. *Proc. SPIE* **4707**, 134–143.

KOZLOVSKAYA, V., ALEXANDER, J. F., WANG, Y., KUNCEWICZ, T., LIU, X., GODIN, B. & KHARLAMPIEVA, E. 2014 Internalization of red blood cell-mimicking hydrogel capsules with ph-triggered shape responses. *ACS Nano* **8** (6), 5725–5737.

KRUEGER, M. & THOM, F. 1997 Deformability and stability of erythrocytes in high-frequency electric fields down to subzero temperatures. *Biophys. J.* **73** (5), 2653–2666.

KWAK, S. & POZRIKIDIS, C. 2001 Effect of membrane bending stiffness on the axisymmetric deformation of capsules in uniaxial extensional flow. *Phys. Fluids* **13** (5), 1234–1242.

LAC, E., MOREL, A. & BARTHÈS-BIESEL, D. 2007 Hydrodynamic interaction between two identical capsules in simple shear flow. *J. Fluid Mech.* **573**, 149–169.

LEE, S. S., YIM, Y., AHN, K. H. & LEE, S. J. 2009*a* Extensional flow-based assessment of red blood cell deformability using hyperbolic converging microchannel. *Biomedical Microdevices* **11** (5), 1021–1027.

LEE, S.-Y., FERRARI, M. & DECUZZI, P. 2009*b* Shaping nano-/micro-particles for enhanced vascular interaction in laminar flows. *Nanotechnology* **20** (49), 495101.

LEVANT, M. & STEINBERG, V. 2016 Intermediate regime and a phase diagram of red blood cell dynamics in a linear flow. *Phys. Rev.* E **94**, 062412.

MCCONNELL, L. C., VLAHOVSKA, P. M. & MIKSIS, M. J. 2015 Vesicle dynamics in uniform electric fields: squaring and breathing. *Soft Matt.* **11**, 4840–4846.

MERKEL, T. J., JONES, S. W., HERLIHY, K. P., KERSEY, F. R., SHIELDS, A. R., NAPIER, M., LUFT, J. C., WU, H., ZAMBONI, W. C., WANG, A. Z., BEAR, J. E. & DESIMONE, J. M. 2011 Using mechanobiological mimicry of red blood cells to extend circulation times of hydrogel microparticles. *Proc. Natl Acad. Sci. USA* **108** (2), 586–591.

MOHANDAS, N. & EVANS, E. 1994 Mechanical properties of the red cell membrane in relation to molecular structure and genetic defects. *Annu. Rev. Biophys. Biomol. Struct.* **23** (1), 787–818.

POZRIKIDIS, C. 1990 The axisymmetric deformation of a red blood cell in uniaxial straining Stokes flow. *J. Fluid Mech.* **216**, 231–254.

POZRIKIDIS, C. 1992 *Boundary Integral and Singularity Methods for Linearized Viscous Flow*. Cambridge University Press.

POZRIKIDIS, C. 2003*a Modeling and Simulation of Capsules and Biological Cells*. Chapman & HALL/CRC.

POZRIKIDIS, C. 2003*b* Numerical simulation of the flow-induced deformation of red blood cells. *Ann. Biomed. Engng* **31** (10), 1194–1205.

POZRIKIDIS, C. 2005 Axisymmetric motion of a file of red blood cells through capillaries. *Phys. Fluids* **17** (3), 031503.

RALLISON, J. M. & ACRIVOS, A. 1978 A numerical study of the deformation and burst of a viscous drop in an extensional flow. *J. Fluid Mech.* **89**, 191–200.

SCHEURICH, P., ZIMMERMANN, U., MISCHEL, M. & LAMPRECHT, I. 1980 Membrane fusion and deformation of red blood cells by electric fields. *Z. Naturforsch.* C **35** (11–12), 1081–1085.

SEBASTIÁN, J. L., MUÑOZ, S., SANCHO, M. & MIRANDA, J. M. 2006 Analysis of the electric field induced forces in erythrocyte membrane pores using a realistic cell model. *Phys. Med. Biol.* **51** (23), 6213–6224.

SECOMB, T. W. 2017 Blood flow in the microcirculation. *Annu. Rev. Fluid Mech.* **49** (1), 443–461.

SHE, S., LI, Q., SHAN, B., TONG, W. & GAO, C. 2013 Fabrication of red-blood-cell-like polyelectrolyte microcapsules and their deformation and recovery behavior through a microcapillary. *Adv. Mater.* **25** (40), 5814–5818.

SHE, S., YU, D., HAN, X., TONG, W., MAO, Z. & GAO, C. 2014 Fabrication of biconcave discoidal silica capsules and their uptake behavior by smooth muscle cells. *J. Colloid Interface Sci.* **426**, 124–130.

SKALAK, R., TOZEREN, A., ZARDA, R. P. & CHIEN, S. 1973 Strain energy function of red blood cell membranes. *Biophys. J.* **13** (3), 245–264.

SUKHORUKOV, V. L., MUSSAUER, H. & ZIMMERMANN, U. 1998 The effect of electrical deformation forces on the electropermeabilization of erythrocyte membranes in low- and high-conductivity media. *J. Membr. Biol.* **163** (3), 235–245.

THOM, F. 2009 Mechanical properties of the human red blood cell membrane at $-15\,^{\circ}\text{C}$. *Cryobiology* **59** (1), 24–27.

THOM, F. & GOLLEK, H. 2006 Calculation of mechanical properties of human red cells based on electrically induced deformation experiments. *J. Electrostat.* **64** (1), 53–61.

TREFETHEN, L. N. 1996 Finite difference and spectral methods for ordinary and partial differential equations. Chapter 7 in unpublished text https://people.maths.ox.ac.uk/trefethen/pdetext.html.

UR, A. & LUSHBAUGH, C. C. 1968 Some effects of electrical fields on red blood cells with remarks on electronic red cell sizing. *Brit. J. Haematology* **15** (6), 527–538.

VENKATARAMAN, S., HEDRICK, J. L., ONG, Z. Y., YANG, C., EE, P. L. R., HAMMOND, P. T. & YANG, Y. Y. 2011 The effects of polymeric nanostructure shape on drug delivery. *Adv. Drug Deliv. Rev.* **63** (14–15), 1228–1246.

VLAHOVSKA, P. M., PODGORSKI, T. & MISBAH, C. 2009 Vesicles and red blood cells in flow: From individual dynamics to rheology. *C. R. Phys.* **10** (8), 775–789.

WOLF, M., GULICH, R., LUNKENHEIMER, P. & LOIDL, A. 2011 Broadband dielectric spectroscopy on human blood. *Biochimica et Biophysica Acta (BBA) - General Subjects* **1810** (8), 727–740.

YAGINUMA, T., OLIVEIRA, M. S. N., LIMA, R., ISHIKAWA, T. & YAMAGUCHI, T. 2013 Human red blood cell behavior under homogeneous extensional flow in a hyperbolic-shaped microchannel. *Biomicrofluidics* **7** (5), 054110.

YAZDANI, A. Z. K., KALLURI, R. M. & BAGCHI, P. 2011 Tank-treading and tumbling frequencies of capsules and red blood cells. *Phys. Rev.* E **83** (4 Pt 2), 046305.

YEN, J.-H., CHEN, S.-F., CHERN, M.-K. & LU, P.-C. 2015 The effects of extensional stress on red blood cell hemolysis. *Biomed. Engng: Applics. Basis Commun.* **27** (05), 1550042.

ZHOU, H. & POZRIKIDIS, C. 1995 Deformation of liquid capsules with incompressible interfaces in simple shear flow. *J. Fluid Mech.* **283**, 175–200.